



1 **Aerosol optical properties derived from POLDER-3/PARASOL (2005-2013) over the**
2 **western Mediterranean Sea: I. Quality assessment with AERONET and in situ**
3 **airborne observations**

4 Paola Formenti^{1,*}, Lydie Mbemba Kabuiku^{1,4}, Isabelle Chiapello², Fabrice Ducos², François Dulac³
5 and Didier Tanré²

6 ¹ Laboratoire Interuniversitaire des Systèmes Atmosphériques, UMR CNRS 7583, Université Paris-
7 Est Créteil et Université Paris Diderot, Institut Pierre-Simon Laplace, Créteil, France

8 ² Laboratoire d'Optique Atmosphérique, UMR CNRS 8518, Université Lille, Villeneuve d'Ascq, France

9 ³ Laboratoire des Sciences du Climat et de l'Environnement, UMR 8212 CEA-CNRS-UVSQ 8212,
10 Institut Pierre-Simon Laplace, Université Paris-Saclay, Gif-sur-Yvette, France

11 ⁴ Agence De l'Environnement et de la Maîtrise de l'Energie (ADEME) 20 avenue du Grésillé,- Angers,
12 France

13

14 * corresponding author (paola.formenti@lisa.u-pec.fr)

15

16 For submission to Atmos. Meas. Tech., ChArMEx special issue

17



18 **Abstract**

19 The western Mediterranean atmosphere is impacted by a variety of aerosol sources, producing a
20 complex and variable mixture of natural and anthropogenic particles, with different chemical and
21 physical properties. Satellite sensors provide a useful global coverage of aerosol parameters but
22 through indirect measurements that request careful validation. Here we present the results of a long-
23 term regional scale analysis of the full dataset (March 2005 and October 2013) of POLDER-
24 3/PARASOL ocean operational retrievals of the total, fine and coarse aerosol optical depth (AOD,
25 AOD_F and AOD_C), Angstrom exponent (AE), and the spherical/non-spherical partition of coarse-mode
26 AOD (AOD_{CS} and AOD_{CNS}), respectively. The evaluation is performed using data from seventeen
27 coastal and insular ground-based AERONET sites on one side, and airborne vertical profiles of
28 aerosol extinction and number size distribution obtained by the SAFIRE ATR 42 aircraft operated in
29 the area during summer 2012 and 2013 on the other side. This study provides the first regional
30 evaluation of uncertainties of the POLDER-3 products, and highlights their quality. The POLDER-3
31 Ångström exponent, representing AOD spectral dependence in link with the aerosol particle size
32 distribution, is biased towards small values. This bias, however, does not prevent using AE for
33 classifying the regional aerosol laden air masses. AOD_F corresponds to particle smaller than 0.6-0.8
34 μm in diameter and appears suitable to monitor the aerosol submicron fraction from space. We also
35 provide an original validation of POLDER-3 AOD_C and its spherical/non-spherical partition, which
36 shows agreement within 25% with AERONET shape retrievals when the aerosol coarse fraction
37 dominates.

38 **1. Introduction**

39 Aerosols include a large variety of particles (mineral dust, sea salt, soot carbon and organic species,
40 sulphates, nitrates...) emitted by natural and anthropic sources and different mechanisms
41 (combustion, wind erosion, gas-to-particle conversion, etc.). Aerosols have a short lifetime in the
42 troposphere (Boucher, 2015) but they are key to many atmospheric processes, as the redistribution
43 of solar and thermal radiation by scattering and absorption, cloud formation and precipitation, and air



44 quality degradation, which, in turn are relevant in shaping the Earth climate and liveability (Pope III et
45 al., 2002; Akimoto, 2003; Pope III and Dockery, 2006; Monks et al., 2009; Boucher et al., 2013).

46 Despite its importance, the global aerosol radiative effect is far from being certain, as both aerosol
47 spatial distribution and optical properties are affected by large unknowns (Boucher et al., 2013; Myhre
48 et al., 2013). Furthermore, the apportionment of aerosols to anthropic and natural sources is critical
49 to evaluate the perturbative forcing of human activities on the Earth radiative budget and ultimately
50 climate (Myhre et al., 2013; Shindell et al., 2013; Kim et al., 2014; Pan et al., 2015). In this general
51 context, the Mediterranean basin is a region of great interest. Submitted to demographic pressure
52 and experiencing bad air quality (Monks et al., 2009; Kovats et al., 2014), the Mediterranean is a high
53 emission and transport region of all kinds of anthropogenic and natural aerosols (e.g. Moulin et al.,
54 1998; Lelieveld et al., 2002; Pace et al., 2005 and 2006; Querol et al., 2009; Pey et al., 2013; Becagli
55 et al., 2017), as well as one of the most vulnerable areas to climate change (Giorgi, 2006), with severe
56 future warming leading to a reduction in precipitations and soil moisture, and henceforth a significant
57 water stress towards the end of the century (Giorgi and Lionello, 2008; García-Ruiz et al., 2011;
58 Christensen et al., 2013).

59 Through the years, the Mediterranean aerosols have been investigated through a number of
60 dedicated local and regional scale experiments (e.g. Söderman and Dulac, 1998; Formenti et al.,
61 2002; Lelieveld et al., 2002; Zerefos et al., 2002; Dulac and Chazette, 2003; Cros et al., 2004; Putaud
62 et al., 2004, Mallet et al., 2016), surface monitoring stations and networks (e.g. Bergametti et al.,
63 1989; Migon et al., 1993; Mihalopoulos et al., 1997; Meloni et al., 2007; di Sarra et al., 2008; Pérez
64 et al., 2008; Querol et al., 2009; Kalivitis et al., 2011; Mallet et al., 2013; Pappalardo et al., 2014;
65 Lyamani et al., 2015) and satellite observations (e.g. Dulac et al., 1992; Moulin et al., 1998; Barnaba
66 and Gobbi, 2004; Antoine and Nobileau, 2006; Papadimas et al., 2008; Gkikas et al., 2009 and 2016).
67 More recently, the regional-scale Chemistry-Aerosol Mediterranean Experiment (ChArMEX,
68 <http://charmex.lsce.ipsl.fr/>) within the international Mediterranean Integrated STudies at Regional And
69 Local Scales (MISTRALS, <http://www.mistrals-home.org>) program has significantly added to the



70 existing body of knowledge by providing new ground-based, airborne and balloon-borne observations
71 over the western part of the basin (Mallet et al., 2016; see also this special issue).

72 ChArMEX has also provided a new momentum in the analysis of regional ground-based and satellite
73 aerosol observations on long and short periods (e.g. Mallet et al., 2013; Nabat et al., 2013; Lyamani
74 et al., 2015; Gkikas et al., 2016; Granados-Muñoz et al., 2016; Sicard et al., 2016). Satellite data are
75 highly valuable to provide information on the regional and global aerosol spatial and temporal
76 distribution and optical properties which are input to climate models. Most satellite instruments (e.g.,
77 MODIS, SEAWIFS, AVHRR, SEVIRI...) retrieve the Aerosol Optical Depth (AOD), representing the
78 column-integrated optically-active content of atmospheric aerosols, and also proportional to the net
79 change in the clear sky outgoing radiative flux at the top of the atmosphere (Boucher, 2015). The
80 AOD is an essential parameter to establish the climatology of the distribution and effects of
81 atmospheric aerosols and it is often used for model evaluation (Nabat et al., 2013). With this respect,
82 advanced spaceborne retrievals deriving the AOD as a function of particle size and shape, and
83 possibly of wavelength, are most useful in evaluating the origin and the radiative effect of aerosols of
84 different nature.

85 In this paper, we present a first comprehensive quality-assessment study of the advanced dataset
86 provided by the operational retrieval ocean algorithm of the third multi-spectral, multi-directional and
87 polarized POLDER-3 (POLarization and Directionality of the Earth's Reflectances) radiometer on
88 PARASOL (Polarization & Anisotropy of Reflectances for Atmospheric Sciences coupled with
89 Observations from a Lidar) satellite (Herman et al., 2005; Tanré et al., 2011) over the western
90 Mediterranean basin. POLDER-3 operated from March 2005 to October 2013 and provided the total,
91 fine and coarse mode aerosol optical depth (AOD, AOD_F and AOD_C) at the wavelength of 865 nm,
92 the spectral dependence of the AOD (Angström Exponent, AE), and the partition of spherical and
93 non-spherical AOD_C (AOD_{CS} and AOD_{CNS}, respectively). This paper extends previous evaluations of
94 AOD and AOD_F (Goloub et al., 1999; Fan et al., 2008; Bréon et al., 2011), and provides the first
95 estimate of the significance of the coarse mode spherical and non-spherical components (AOD_C,
96 AOD_{CS} and AOD_{CNS}).



97 This study is based on comparisons with co-localised observations from the sun/sky photometers of
98 coastal and insular stations of the Aerosol Robotic Network (AERONET; Holben et al., 1998), and
99 with the in situ measurements of vertical profiles of aerosol extinction and size distribution which were
100 performed by the French ATR 42 environmental research aircraft of the Service des Avions Français
101 Instrumentés pour la Recherche en Environnement (Safire, www.safire.fr) during the ChArMEx
102 intensive campaigns (Di Biagio et al., 2016, Denjean et al., 2016, Mallet et al., 2016). In particular,
103 the use of the size distribution vertical profiles measured in situ allows us to calculate the aerosol
104 optical depth over different size ranges, and the evaluation of AOD_F and AOD_C .

105 The analysis presented in this paper is essential to geophysical analyses of observations by
106 POLDER-3 of the spatial and temporal variability of the aerosol load over the western Mediterranean
107 basin.

108 **2. Measurements**

109 **2.1. POLDER-3/PARASOL**

110 The third radiometer POLDER-3 on PARASOL, operational from March 2005 to October 2013, was
111 part of the A-Train constellation operated on a sun-synchronous orbit at 705 km crossing the Equator
112 at 13:30 (Equator local time) (Tanré et al., 2011). In December 2009, it left the A-Train, and continued
113 the observations at 3.9 km below, and at 9.5 km below in 2011. This changed its hour of passage,
114 which was 16:00 Equator local time at the end of the operational period.

115 POLDER-3/PARASOL used a 274 x 242-pixels CCD detector array, each pixel covering 5.3 x 6.2 km²
116 at nadir. The size of the POLDER-3 images was 2100 x 1600 km², allowing to achieve a global
117 coverage within two days. The western Mediterranean area could be covered in less than 5 minutes
118 along its north-to-south axis. The spatial resolution of POLDER-derived (Level 2) aerosol parameters
119 is about 18.5 x 18.5 km² (corresponding to 3 x 3 pixels of the Level-1 grid; [http://www.icare.univ-](http://www.icare.univ-lille1.fr/parasol/products)
120 [lille1.fr/parasol/products](http://www.icare.univ-lille1.fr/parasol/products)).

121 The instrument measured solar radiance at 9 wavelengths from 443 to 1020 nm, three of which with
122 polarisation (490, 670, 865 nm), and at up to 16 different angles ($\pm 51^\circ$ along, $\pm 43^\circ$ across track).



123 Cloud screening according to Bréon and Colzy (1999) was applied to minimize possible cloud
124 contamination of aerosol products.

125 In this paper, we used the latest algorithm update (collection 3) performed in 2014 of the operational
126 clear-sky ocean retrieval algorithm (Deuzé et al., 1999, 2000; Herman et al., 2005). This latest version
127 includes calibration improvements and uses the total and polarized radiances at 670 and 865 nm. For
128 each clear sky pixel, the algorithm recalculates the observed polarized radiances at several
129 observational angles from a Look-Up Table (LUT) built on aerosol micro-physical models. These are
130 constructed as follows: (i) aerosol are not-absorbing, that is, the imaginary part m_i of their complex
131 refractive index ($m = m_r - i m_i$) is nul. Only the real part m_r is attributed, and considered as invariant
132 with wavelength between 670 and 865 nm; (ii) the aerosol number size distribution is bimodal and
133 lognormal with a fine mode with effective diameter (D_{eff}) smaller than 1.0 μm and a coarse mode with
134 D_{eff} larger than 1.0 μm . The coarse mode includes a non-spherical fraction based on the spheroidal
135 model from Dubovik et al. (2006). Collection 3 increases the number of modes with respect to the
136 previous versions reported by Herman et al. (2005) and Tanré et al. (2011), and allows spheroidal
137 D_{eff} to take two values (2.96 or 4.92 μm). The summary of LUT parameters are presented in the
138 supplementary material (**Table S1**).

139 The calculations of the multi-spectral, multi-angle polarized radiances are done using a Mie model for
140 homogeneous spherical particles or the spheroidal optical model developed by Dubovik et al. (2006).
141 A quality flag index (0 indicating the lowest and 1 the highest quality) is attributed to each pixel
142 depending on the quality of radiance simulation.

143 In this paper, we target the following POLDER-3 oceanic (i.e. over ocean surfaces) aerosol products,
144 in which AODs are at 865 nm:

- 145 • The total aerosol optical depth (AOD), and the Ångström Exponent (AE) representing the
146 spectral dependence of AOD, and calculated as

147

148
$$\text{AE} = - \frac{\ln(\text{AOD}_{865}/\text{AOD}_{670})}{\ln(865/670)} \quad (1)$$



149

- 150 • The aerosol optical depth due to the fine particle mode (AOD_F)
- 151 • And the aerosol optical depth due to the spherical (AOD_{CS}) and non-spherical (AOD_{CNS}) coarse
152 mode fractions, obtained for clear-sky pixels with favourable viewing geometries (scattering
153 angles between 90° and 160°). These products allow estimating the fraction of non-spherical
154 particles in the coarse mode AOD (f_{CNS}) from

$$155 \quad f_{CNS} = AOD_{CNS} / (AOD_{CNS} + AOD_{CS}) \quad (2)$$

156 Whereas AOD_F was available for all clear-sky pixels regardless of the geometry of observations, the
157 AOD_C was estimated in two ways depending on the availability of observations. For days with
158 observations in favourable viewing geometrical conditions, AOD_C was calculated as the sum of
159 measured AOD_{CS} and AOD_{CNS} . For the remaining days, AOD_C was calculated as $AOD - AOD_F$. A
160 maximum difference of ± 0.002 rounding errors was found for days when both methods are applicable.

161 Only the POLDER-3 aerosol products from pixels with a quality flag index ≥ 0.5 have been considered
162 in the following discussion.

163 2.2. AERONET

164 AERONET is a global network of ground-based multi-spectral sun/sky photometers (Holben et al.,
165 1998; 2001) dedicated to real time monitoring of aerosol properties and widely used as ground-based
166 reference for validation of aerosol satellite retrievals (e.g., Goloub et al., 1999; Bréon et al., 2011). It
167 uses standardized sun/sky photometers (CIMEL CE-318, Cimel Electronique, Paris) measuring solar
168 extinction and sky radiances (at times with polarization) in the almucantar plane at wavelengths
169 between 340 and 1020 nm (most commonly 440, 675, 870, and 1020 nm), that allow deriving a
170 number of aerosol optical and microphysical parameters (Dubovik and King, 2000; Dubovik et al.,
171 2006).

172 AOD and AE are obtained about every 15 minutes from the measurement of the direct sun extinction
173 and are reported as the average of a triplet of acquisitions lasting approximately 30 s. For freshly
174 calibrated and well maintained instruments, the accuracy in AOD is of the order of 0.01-0.02



175 regardless of the AOD value (Holben et al., 1998). The aerosol optical depth in the fine and coarse
176 mode (AOD_F and AOD_C , respectively) are recalculated from the column-integrated volume size
177 distribution retrieved by the inversion algorithm described in Dubovik and King (2000) and Dubovik et
178 al. (2006). The fine and coarse modes of the retrieved volume size distribution are defined as the
179 modes below and above a threshold diameter ($D_{cut-off}$) corresponding to the minimum of the size
180 distribution. The $D_{cut-off}$ value can vary between 0.44 and 0.99 μm . AOD_F and AOD_C values are
181 estimated by recalculating the extinction due to the fine and coarse modes of the aerosols. The latest
182 AERONET retrieval scheme considers an aerosol mixture of polydisperse, randomly-oriented
183 homogeneous spheroids with a fixed distribution of aspect ratios (Mishchenko et al., 1997) and
184 provides fraction (in percentage) of non-spherical/spherical particles, i.e. f_{NS}/f_S (Dubovik et al., 2006).
185 By clear sky, there are about 10 measurements per day of this fraction in the early day or late
186 afternoon (solar zenith angle $\geq 50^\circ$).

187 We used AERONET V2 level-2 quality assured aerosol products. Seventeen coastal AERONET
188 stations, shown in **Figure 1**, were selected in this study, (see also **Table 1** for their respective
189 geographical coordinates and covered periods). Their regional distribution covers the entire western
190 Mediterranean basin, including south Europe (e.g., near coastal stations of Barcelona, Toulon,
191 Villefranche-sur-Mer...), North Africa (Blida), and island locations in the northern (Ersa), central
192 (Palma de Mallorca) and southern (Lampedusa and Alboran) basin, therefore capturing the diversity
193 of the aerosol population, resulting from the different sources contributing to the Mediterranean
194 aerosol (desert dust, marine, urban and industrial pollution, and biomass burning). The dataset also
195 includes the ground-based super-sites of Ersa and Lampedusa of the ChArMEx project (Mallet et al.,
196 2016). Considering the 17 stations altogether, more than 18000 daily observations of AOD are
197 available in total in both POLDER-3 and AERONET datasets, among which 6421 are concurrent (see
198 section 3.2 below) and thus available for comparison. We did not consider for tentative matching with
199 POLDER in this study a rather limited number (<100) of daily observations obtained from manual sun
200 photometers on-board ships in our area (Figure 1) and period of interest, which are also available
201 from the Maritime Aerosol Network component of AERONET (Smirnov et al., 2011).



202 **2.3. ChArMEx airborne measurements**

203 The airborne measurements relevant to this paper were performed on the French ATR 42
204 environmental research aircraft of Safire during two of the intensive observational periods of the
205 ChArMEx project:

- 206 • The Transport and Air Quality (TRAQA) campaign, dedicated to the study of air pollutants
207 transport from Europe to the Mediterranean, their evolution and their impact on regional air
208 quality (Di Biagio et al., 2015; 2016; Nabat et al., 2015a; Rea et al., 2015);
- 209 • The Aerosol Direct Radiative Forcing on the Mediterranean (ADRIMED) campaign was
210 dedicated to the characterization of aerosol optical properties in the Mediterranean and their
211 direct radiative effect in clear sky conditions (Denjean et al., 2016; Mallet et al., 2016).

212 During TRQA, the ATR 42, based at the Franczal airport near Toulouse, France (43°36'N, 1°26'E),
213 conducted 17 flights from 20 June to 13 July 2012 encountering weather conditions favouring the
214 transport of pollution aerosols from continental Europe, and particularly from the Rhone valley, the
215 Gulf of Genoa and Barcelona, giving raise to AOD values in the range of 0.2-0.6 at 550 nm over the
216 northwestern Mediterranean. From 17 to 23 June, and then on 29 June, two episodes of desert dust
217 transport were observed in the free troposphere, increasing the AOD up to 1.4 on June 29. (Di Biagio
218 et al., 2015; 2016). During ADRIMED, the ATR 42, based in Cagliari, Italy (39°15'N, 9°03'E), flew 16
219 scientific flights between 14 June and 4 July 2013 (Denjean et al., 2016; Mallet et al., 2016). Several
220 episodes of desert dust transport from southern Algeria and Morocco and northern Algeria and Tunisia
221 were observed over the western and central Mediterranean, particularly off the Balearic Islands and
222 above the Lampedusa island offshore Tunisia (Denjean et al., 2016). The total optical depth at 550 nm
223 remained moderate, in the order of 0.2-0.4 even during dust events (Mallet et al., 2016).

224 **2.3.1. Airborne instrumentation measuring aerosol optical properties**

225 **2.3.1.1. PLASMA photometer**

226 PLASMA (Photomètre Léger Aéroporté pour la Surveillance des Masses d'Air), developed by LOA
227 (Laboratoire d'Optique Atmosphérique, Lille), is a multi-spectral sunphotometer which measures the



228 direct sun radiance and retrieves the AOD at 15 wavelengths between 343 and 2250 nm, including
229 869 nm (Karol et al., 2013). The estimated uncertainty ranges between 0.005 and 0.01 (Karol et al.,
230 2013). PLASMA was operated during the ADRIMED campaign only, when it was mounted on the roof
231 of the ATR 42, allowing the retrieval of a vertical profile of both the spectral AOD and the aerosol
232 particle size distribution (Torres et al., 2017).

233 **2.3.1.2. CAPS-PMex**

234 The Cavity Attenuated Phase Shift in situ instrument (CAPS-PMex, Aerodyne Research Inc.)
235 measures the extinction coefficient σ_{ext} at 532 nm with an estimated relative uncertainty of $\pm 3.2\%$
236 (Kebabian et al., 2007; Massoli et al., 2010; Petzold et al., 2013). The operating principle is based on
237 the modulation of the frequency and the phase changes of the light emitted by a LED source due to
238 aerosols, after correction of the Rayleigh scattering by the molecules present in the air mass. As
239 described in Denjean et al. (2016), the instrument was available during the ADRIMED campaign only,
240 when it was located inside the cabin behind the Communautary Aerosol Inlet (CAI), and operated at
241 0.85 L min^{-1} and with a temporal resolution of 1 second. In this paper, the extinction coefficient σ_{ext} is
242 expressed in Mm^{-1} ($1 \text{ Mm}^{-1} = 10^{-6} \text{ m}^{-1}$).

243 **2.3.1.3. Nephelometer**

244 The scattering coefficient σ_{scatt} at 450, 550 and 700 nm was measured by a spectral integrating
245 nephelometer (model 3563, TSI Inc.) described extensively by Anderson et al. (1996) and Anderson
246 and Ogren (1998). During both TRAQA and ADRIMED, the instrument was operated at 30 L min^{-1}
247 with a temporal resolution of 1-2 seconds downstream the AVIRAD inlet also onboard the ATR 42 (Di
248 Biagio et al., 2015; 2016; Denjean et al., 2016). The AVIRAD inlet estimated size cut-off,
249 corresponding to the diameter at which particles are collected with a 50% efficiency, is $12 \mu\text{m}$ in optical
250 diameter.

251 The instrument uses a halogen lamp as light source and three photomultipliers preceded by spectral
252 filters. Due to the geometry of its sensing volume, the nephelometer measures the scattering
253 coefficient (σ_{scatt}) between 7° and 170° and the backscattering coefficient (σ_{bscatt}) between 90° and



254 170°. The scattering Angström exponent AE_{scatt} and representing the scattering spectral dependence
255 can be calculated as

256

$$257 \quad AE_{\text{scatt}} = -\frac{\ln(\sigma_{\text{scatt},450}/\sigma_{\text{scatt},700})}{\ln(450/700)} \quad (3)$$

258

259 The relative uncertainty in σ_{scatt} due to calibration, counting statistics and non-idealities of detector
260 surfaces, is estimated to be $\pm 1\text{-}2\%$ for submicron aerosols and $\pm 8\text{-}15\%$ for supermicron aerosols
261 (Müller et al., 2009). To these values usually adds the error related to the geometric truncation of the
262 measured angular range of the scattering phase function due to the sensing volume (Anderson and
263 Ogren, 1998). This truncation induces an underestimation of σ_{scatt} and σ_{bscatt} , which depends on the
264 angular distribution of the scattered light, and thus on particle size. Anderson and Ogren (1998) have
265 shown that the uncertainty induced by the underestimation of σ_{scatt} can be parameterized by the
266 scattering spectral dependence for submicron aerosols. This parameterization is not possible for
267 aerosols of larger size (diameter greater than 1 μm), because the Angström coefficient tends to zero
268 whereas the underestimation is important (50-60%) because of the increase of the forward scattering.
269 In this case, the correction is performed by optical calculation if the particle size distribution and
270 refractive index are known (Müller et al., 2009; Formenti et al., 2011). As for σ_{ext} , in this paper σ_{scatt} is
271 expressed in Mm^{-1} .

272 2.3.2. Aerosol particle size distribution

273 Because of its extent, the aerosol particle size distribution is measured in situ by the combination of
274 several instruments, often based on different physical principles (Wendisch and Brenguier, 2013). In
275 our work, we used a combination of different optical counters operating on the fine and coarse modes
276 of the aerosols, that is:

- 277 • a Passive Cavity Aerosol Spectrometer Probe (PCASP, Droplet Measurement Technologies,
278 Boulder, Colorado), operated at 632.8 nm with a temporal resolution of 1 second. The PCASP



279 measures light scattering between 35 and 135° to derive the particle number size distribution
280 over 31 channels between 0.1 and 3.0 µm in diameter (Liu et al., 1992; Reid et al., 1999). The
281 PCASP was operated on a wing pod of the ATR 42 during the TRAQA campaign only.

282 • an Ultra High Sensitivity Aerosol Spectrometer (UHSAS, Droplet Measurement Technologies,
283 Boulder, Colorado), operated at 1054 nm with a temporal resolution of 1 second. The UHSAS
284 measures light scattering between 22 and 158° to derive the particle number size distribution
285 over 99 size channels between 0.04 and 1.0 µm in diameter (Cai et al., 2008). The UHSAS
286 replaced the PCASP under the aircraft wing during the ADRIMED campaign.

287 • a Sky-Grimm counter (1.129 model, Grimm Aerosol Technik; Grimm and Eatough, 2009),
288 operated at 632.8 nm with a temporal resolution of 6 seconds. The instrument integrates light
289 scattering between 30° and 150° to derive the particle number size distribution over 32
290 channels between 0.25 and 30µm in diameter (Grimm and Eatough, 2009). The instrument
291 was available during both TRAQA and ADRIMED, operated inside the aircraft cabin and
292 behind the AVIRAD inlet. Due to a flow problem, measurements during TRAQA are restricted
293 to the portions of the flights when the ATR 42 remained below 350 m above sea level.

294 3. Validation strategy

295 3.1. Matching POLDER-3 and in situ aircraft measurements

296 In situ aircraft measurements provided direct and indirect observations for validation. Direct
297 observations of the total AOD were obtained by the reading of the PLASMA sun photometer for those
298 portions of the flights when the ATR 42 flew at its lowest altitude and by integrating the vertical profile
299 of the extinction coefficient σ_{ext} measured by the CAPS-PMex instrument between the minimum and
300 the maximum heights (z_{min} and z_{max}) of the ATR 42 during profile ascents or descents.

301 Indirect validation of the size-dependent optical depth (AOD, AOD_F and AOD_C) was performed by
302 optical calculation from the number size distribution $dN(D,z)/d\log D$ measured by the combination of
303 the PCASP, UHSAS and Grimm optical counters as

304



$$305 \quad \text{AOD}_x(865 \text{ nm}) = \int_{z_{\min}}^{z_{\max}} dz \sigma_{\text{ext}}(z) = \int_{z_{\min}}^{z_{\max}} dz \int_{D_x'}^{D_x} \pi D^2 Q_{\text{ext}}(z, D, m) \frac{dN(D, z)}{d \log D} d \log D \quad (4)$$

306

307 The suffix x in Equation 4 indicates the size domain of the aerosol optical depth (total, fine or coarse)
308 considered in the calculations.

309 Equation 4 allows one to estimate the aerosol optical depth over a variable size domain, whose
310 boundaries (D_{\min} and D_{\max}) can be adjusted to represent the fine and the coarse modes, as well as
311 the total particle size distribution.

312 The iterative procedure used for the calculation is presented in **Figure 2**. All calculations used the
313 optical Mie theory for homogeneous spherical particles (Mie, 1908). The initial step of the procedure
314 consisted in estimating the aerosol number size distribution, input of Equation 4, from the
315 measurements of the PCASP, UHSAS and Grimm optical counters operated on board the ATR 42
316 during TRAQA and ADRIMED. This required two actions, described in details in the Supplementary
317 material.

318 1. The conversion of the nominal "optical equivalent spherical diameter" (D_{EO}) characteristic of
319 each particle counter to a "geometric equivalent spherical diameter" (D_{EG}). The operating
320 principle of the particle optical counters is based on the angular dependence of the light
321 scattering intensity to the particle size (Wendisch and Brenguier, 2013). The proportionality
322 factor between angular light scattering and particle size depends on the particle complex
323 refractive index. At calibration, the optical particle counters provide with "an optical equivalent
324 spherical diameter" (D_{EO}), corresponding to the diameter of standard material, generally
325 spherical latex beads, which refractive index ($m_{\text{latex}} = 1.59 - 0i$) is usually different from the real
326 aerosol refractive index measured in atmosphere. It is therefore necessary to convert the
327 measured D_{EO} value into a so-called "geometric equivalent spherical diameter" (D_{EG}) value
328 taking into account the actual refractive index of ambient particles.

329 2. The combination of measurements over different size ranges. Since no optical counter
330 completely covers the full size range of atmospheric aerosols, measurements of the PCASP,



331 UHSAS and Grimm were combined by examining their agreement on their size overlap
332 domains. When successful, the particle number size distribution obtained by the combination
333 was normalised to the total particle number and fitted using a multi-mode lognormal
334 distribution to eliminate discontinuities and extend the representation beyond the lower and
335 upper operating size ranges of the optical counters.

336 The capability of the derived number size distributions to represent the aerosol extinction coefficient,
337 henceforth to estimate aerosol optical depth, was assessed by comparing the calculated extinction
338 and scattering coefficients σ_{ext} and σ_{scatt} to the measurements of the CAPS-PMex and the
339 nephelometer at 450, 532, 550 and 700 nm. The scattering coefficient σ_{scatt} was calculated by
340 integrating the scattering phase function between 7° and 170° , corresponding to the aperture of the
341 sensing volume of the nephelometer.

342 All optical calculations performed in this paper assumed the spectral complex refractive index m ,
343 representing the aerosol composition, as independent of size. An initial dataset per aerosol type was
344 chosen (Table S2 in the Supplementary material). The calculations were iterated by varying the initial
345 values of the complex refractive indices until both 1/ the adjusted value for the calculation of the
346 extended size distributions and 2/ the comparison between calculations and measurements of the
347 extinction and scattering coefficients agreed within errors. Results of these comparisons are
348 presented in the Supplementary material.

349 **3.2. Constitution of the data set**

350 This section describes the choices of temporal and spatial coincidences adopted for the comparisons
351 between POLDER-3, AERONET and in situ data.

352 **3.2.1. Coincidence with AERONET**

353 As described in previous evaluation studies of aerosol products derived from satellites (e.g., Bréon et al.,
354 2011), two approaches can be considered in order to compare coincident ground-based
355 photometer and satellite aerosol data. One option is to select only the closest (in time) photometer
356 measurement and the closest (in distance) satellite pixel from the photometer site. Another method



357 consist in performing averaging within a certain time window for photometer data, and a spatial
358 average of the satellite data within a given distance from the photometer site. Bréon et al. (2011) have
359 shown that these two approaches give very comparable results for POLDER-3 aerosol products over
360 oceans. In this study we adopted the second approach, considering the POLDER-3 aerosol products
361 from pixels within $\pm 0.5^\circ$ around the AERONET sites. For AERONET AOD and AE, the averaging
362 temporal window was set to ± 1 h around the time of the POLDER-3 passage. For AERONET AOD_F,
363 AOD_C, and shape retrieval, this temporal window produces an insufficient number of data, in particular
364 for springs and summers in the period 2005-2011 due to the temporal time shift of the POLDER-3
365 passage towards the afternoon. Instead, the averaging temporal window was extended to the whole
366 afternoon (that is, all data points later than 12:00 UTC) in order to allow for a significant dataset for
367 comparison.

368 **Table 1** reports the number of available observational days for POLDER-3 and AERONET aerosol
369 parameters at each station in the period March 2005-October 2013, as well as the number of
370 coincident days obtained between POLDER-3 and AERONET. The stations are ranged regarding the
371 number of coincident days obtained for AOD and AE, this number representing the upper limit of the
372 number of common POLDER-3/AERONET observations days available. Including all 17 stations,
373 18634 occurrences of comparable POLDER-3 and AERONET observations are available for AOD,
374 AE, AOD_F and AOD_C, and 7923 occurrences for AOD_{CS} and AOD_{CNS}, due to specific constraints on
375 geometric conditions in the POLDER-3 algorithm necessary to derive shape-related parameters (non
376 sphericity). Per site, the number of clear sky observational days for POLDER-3-derived AOD, AE,
377 AOD_F and AOD_C varies from 668 to 1392. Part of this variability also depends on the percent of sea
378 pixels in the $1^\circ \times 1^\circ$ area around the sites, which is lower for coastal (e.g., Burjassot or Roma) than
379 insular stations (e.g., Alboran, Lampedusa or Gozo). Between 1 pixel in the case of inland stations of
380 Roma and Burjassot, and up to 29 pixels in the case of the small remote island of Alboran were
381 considered. Overall, the number of available AERONET observation days is important both for AOD
382 and AE (18223), and AOD_F and AOD_C (11228). The number of days with AERONET-derived f_{NS} was



383 less significant (4976 data points), due to additional constrains in the inversion necessary to derive
384 this parameter.

385 The number of available AERONET observations per site varied from 158 to 2059 for AOD and AE,
386 and from 43 to 1333 for AOD_F and AOD_C, mainly due to partial functioning of the instruments or
387 maintenance of the sites. At some stations, measurements started years after the beginning of
388 POLDER-3 mission (e.g., 2011 for Alboran, 2013 for Gozo). Finally, the number of POLDER-
389 3/AERONET coincident days available for analysis is 6421 for AOD and AE, 3855 for AOD_F and
390 AOD_C, and 730 for the percentage of spherical coarse particles (f_{NS}).

391 **3.2.2. Coincidence with airborne observations**

392 The comparison between POLDER-3 and airborne measurements was conducted for profile ascents
393 or descents of the ATR 42 close in time with POLDER-3 overpasses. Flight tracks and profiles
394 locations are shown in **Figure 3**, whereas additional details (dates, geographical coordinates, altitude
395 span and duration) are given in **Table 2**. Data from the PLASMA sunphotometer, operated only during
396 ADRIMED, were available only on 8 profiles (also indicated in Table 2) for which the minimum flight
397 altitude was as close as possible to the surface. The data set was limited to ATR 42 profiles extending
398 as much as possible over the column. To evaluate whether the aircraft profile sampled entirely or only
399 partially the aerosol layers, we compared the AOD measured by PLASMA to that obtained by
400 integrating the extinction profile of the CAPS-PMex instrument (not shown). By examining the
401 AERONET time series, we also excluded episodes when the AOD had significantly varied in time
402 between the POLDER-3 overpass and the aircraft profile. This mostly happened for cases when the
403 aerosol optical depth exceed 0.2 due to the transport of mineral dust (flights T-V22 and T-V23 during
404 TRAQA and V31-S3 and V42-S2 during ADRIMED). The profiles discarded for comparison with
405 POLDER-3 were used for the validation of the optical calculations presented in section 4 (not shown
406 in Table 2 nor Figure 3).

407 Prior to analysis, all in situ airborne data were synchronised and then averaged to 30 seconds to
408 reduce the noise due to the native resolution of the measurements (1 to 6 seconds). POLDER-3 data
409 were averaged over pixels within $\pm 0.5^\circ$ around the lowest altitude of each profile. In order to analyse



410 the aerosol vertical stratification, we examined the magnitude of the scattering coefficient σ_{scatt} at 550
411 nm as a function of altitude and its spectral behaviour, represented by the scattering Angström
412 Exponent (AE_{scatt}) measured by the airborne nephelometer. As in previous similar studies (Pace et
413 al., 2006; Formenti et al., 2011; Di Biagio et al., 2015; 2016; Denjean et al., 2016), the aerosol layers
414 were classified in four categories (clear/background maritime, desert dust, pollution, and mixture),
415 following the criteria reported in **Table 3**. The mixture category, indicating mixing between desert dust
416 and pollution, as observed by Denjean et al. (2016), was further detailed to distinguish dust-dominated
417 layers (AE_{scatt} between 0.5 and 0.75) and pollution-dominated layers (AE_{scatt} between 0.75 and 1).

418 3.3. Statistical indicators

419 The agreement between the POLDER-3, AERONET and airborne datasets was quantified by several
420 evaluation metrics, including the number of matchups (N), the linear correlation coefficient (R), the
421 slope (S) and intercept (I) of the linear regression, the root mean square error (RMS), and the bias
422 (B), representing their mean difference.

$$423 \quad \text{RMS} = \sqrt{\frac{1}{n} \sum_{i=1}^n (y_i - x_i)^2} \quad (5)$$

$$424 \quad B = \frac{1}{n} \sum_{i=1}^n (y_i - x_i) \quad (6)$$

425 where x and y are generic datasets, and n the number of pairs of compared values.

426 Additional metrics is provided by the “fraction of accurate retrievals” (G_{frac}) defined by Bréon et al.
427 (2011). This quantity is defined as

428

$$429 \quad G_{\text{frac}} = \frac{\#\text{obs}(\Delta < \text{EE})}{\#\text{obs}} \quad (7)$$

430

431 and quantifies the fraction of POLDER-3 data points for which the absolute difference (Δ) between
432 reference and evaluated data is lower than the estimated error (EE).

433 In accordance to Bréon et al. (2011), EE was calculated as



434

435
$$EE = \pm (0.03 + 0.05 \times AOD) \quad (8)$$

436

437 and applied to all the AOD advanced products. Because G_{frac} is only appropriate for large datasets
438 whose number of data points exceeds 100 (Bréon et al., 2011), it was calculated only for comparisons
439 with AERONET data.

440 4. Results

441 4.1. Evaluation of the total aerosol optical depth

442 **Figure 4** shows the results of comparison of the AOD retrieved by POLDER-3 between 2005 and
443 2013 with respect to the 6421 observations at the seventeen AERONET stations and those on the
444 vertical profiles of the ChArMEx campaigns (PLASMA sunphotometer and calculations from the in
445 situ size distributions).

446 The comparison with AERONET shows a good correlation (regression coefficient $R = 0.88$, $G_{frac} =$
447 73%), with a statistically low dispersion and bias ($RMS = 0.04$, $B = 0.003$). Twenty-seven percent of
448 the observations do not meet the criteria of the G_{frac} parameter. Cases outside the G_{frac} boundary were
449 characterized by large standard deviations, either because the spatial distribution of AOD was
450 heterogeneous in the $1^\circ \times 1^\circ$ area of the pixels surrounding the AERONET sites, or because it varied
451 significantly on the time window of ± 1 hour around the POLDER-3 overpass. In our dataset, the
452 highest value of AOD measured by POLDER-3 was $1.4 (\pm 0.1)$ during a desert dust transport event
453 over Lampedusa observed on April 25, 2011. This is the only event coincident with an AERONET
454 measurement (1.50 ± 0.06) with POLDER-3 AOD > 1 .

455 Figure 4 also shows the comparison with the PLASMA observations and with the calculations initiated
456 by the measured airborne number size distributions.

457 On those, the AOD did not exceed 0.2, whereas AE ranged from 0.31 ± 0.07 to 1.09 ± 0.08 , indicating
458 that these cases are representative of aerosols of different origins. The comparison was also very
459 satisfactory and confirmed the more extensive results from the comparison with AERONET-derived



460 AODs. POLDER-3 provides higher values of AOD for mineral dust (lowest AE values) compared to
461 those calculated from in situ aerosol measurements, which could reflect an underestimate of the
462 coarse mode distribution from the in situ aircraft measurements. On the other hand, POLDER-3 tends
463 to underestimate AOD with respect to PLASMA at low AE values, resulting in a negative bias of the
464 correlation (bias = -0.02). In both cases, the RMS remained low and below 0.05.

465 4.2. Evaluation of fine and coarse aerosol optical depth

466 4.2.1. Comparison with AERONET observations

467 **Figure 5** shows the comparison between POLDER-3 and AERONET for AOD_F and AOD_C . AOD_F
468 remained below 0.25, smaller than AOD_C , which reached 0.8. The correlation coefficient for AOD_C (R
469 = 0.81) is closer to the correlation coefficient for AOD (0.88) than that for AOD_F (0.63). The agreement
470 between POLDER-3 and AERONET is confirmed by the G_{frac} values of 74% for AOD_C and 88% for
471 AOD_F , the low statistical bias (-0.007 for AOD_F and 0.01 for AOD_C), and the moderate dispersion
472 (RMS values between 0.02 for AOD_F and 0.04 for AOD_C). The weaker correlation and the dispersion
473 observed for AOD_F can be attributed to the difficulty in retrieving low values of optical depth.
474 Additionally, Tanré et al. (2011) pointed out that differences could arise by the definitions of the cut-
475 off diameter ($D_{cut-off}$) used in the POLDER-3 and AERONET retrievals to estimate AOD_F . In the
476 AERONET retrievals, AOD_F is calculated from the fine mode of the particle size distribution defined
477 for a value of $D_{cut-off}$ forced between 0.44 and 0.99 μm . In the POLDER-3 algorithm, AOD_F is calculated
478 from the full particle size distribution of the retrieved fine mode, without cut-off. However, because of
479 its use of polarisation, POLDER-3 is the most sensitive to particles smaller than 0.6-0.8 μm in
480 diameter (Tanré et al., 2011 and references therein).

481 In **Figure 6**, we explore the relevance of this difference in the comparison of AOD_F and AOD_C by
482 further separating days when AERONET $D_{cut-off} < 1.0 \mu\text{m}$ and days when $D_{cut-off} \geq 1.0 \mu\text{m}$. The
483 threshold value of 1.0 μm corresponds to the D_{eff} of all the fine modes in the POLDER-3 LUT. Cases
484 with $D_{cut-off} < 1.0 \mu\text{m}$ were more numerous (2413 days), and showed a better agreement (Bias = -
485 0.003, $G_{frac} = 91\%$, RMS = 0.02, $R = 0.60$). Data corresponding to $D_{cut-off} \geq 1.0 \mu\text{m}$ were less numerous
486 (1442 days). Whereas the correlation improved slightly ($R = 0.69$ versus $R = 0.60$), the dispersion



487 increased (bias = -0.01, RMS = 0.03) due to the appearance of points for which AERONET AOD_F
488 almost doubled that of POLDER-3. Colouring the data points by AE showed that the data points with
489 D_{cut-off} below 1.0 μm mostly corresponded to aerosols with a weak-to-moderate spectral dependence
490 (low AE), whereas cases with D_{cut-off} above 1.0 μm mostly (but not exclusively) corresponded to
491 aerosols with a moderate-to-strong spectral dependence (high AE).

492 The size cut-off definition also affects the comparison for AOD_C. For D_{cut-off} <1.0 μm, AOD_C values
493 were high and the correlation was significant. Conversely, AOD_C remained low (≲0.2) when D_{cut-off}
494 ≥1.0 μm. This is consistent with the fact that the contribution of AOD_C to AOD decreases as the D_{cut-}
495 off increases (**Figure S1** in the supplementary material). **Figure 6** shows that discriminating data on
496 the basis of D_{cut-off} results in attributing AOD_F and AOD_C to different aerosol types.

497 **4.2.2. Comparison with airborne measurements**

498 To understand further the previous comparisons, POLDER-3 AOD_F and AOD_C were recalculated from
499 the measured number size distributions (Equation 4) by varying the lower limit of the size integration
500 between 0.4 and 1.0 μm in diameter with a step of 0.2. Results are shown in **Figure 7**. As expected,
501 the comparison for AOD_F is very sensitive to the size range. The best agreement between the
502 retrieved and the calculated AOD_F is obtained for D_{cut-off} between 0.6 and 0.8 μm, both showing high
503 correlation coefficient R and low RMS. Conversely, the AOD_C comparison is almost independent of
504 the value of D_{cut-off} but more affected by the upper limit of the size range in Equation 4.

505 **4.3. Evaluation of the Ångström Exponent**

506 **Figure 8** shows the comparison of AE retrieved by POLDER-3 with values obtained by AERONET,
507 PLASMA and the optical calculations. The comparison with AERONET was restricted to days when
508 the POLDER-3 AOD exceed 0.1 (2031 out of the 6421 data points) to take into account only those
509 values with relative uncertainties within 50%. The comparison showed a significant spread and a
510 moderate correlation coefficient (R = 0.70). However, POLDER-3 tends to underestimate values of
511 AE larger than 1 with respect to AERONET, and overestimate values smaller than 0.5, yielding a
512 significant bias (-0.11). The values obtained by POLDER-3 compare well with the airborne



513 observations of PLASMA ($R = 0.84$), but less well to the optical calculations ($R = 0.42$). In both cases,
514 the bias is positive (0.1 with PLASMA and 0.2 with in situ AE). This fact, observed previously by
515 Goloub et al. (1999) and Tanré et al. (2011), can be explained by considering that the values of AE
516 are calculated from the retrieved AOD at 865 and 670 nm (Equation 1), which, in the ocean retrieval
517 algorithm of POLDER, is obtained by the fit of measured radiance. The current aerosol models in the
518 LUT (modal diameters and real part of the refractive index) provide AE values in the range -0.18 to
519 3.3 . However, the extreme values are obtained only if the size distribution allowing to match the
520 observed radiances consists of a single mode of non-spherical coarse particle (modal diameter of 0.9
521 μm for $\text{AE} = -0.18$) or a single mode of fine spherical particles (modal diameter of 0.08 μm for $\text{AE} =$
522 3.3). **Figure 9** compares the scatterplots of AE and AOD obtained for the coincident POLDER-3 and
523 AERONET datasets. The tendency of POLDER-3 to underestimate AE shows up clearly by the
524 absence of values of AE larger than 2.5 , which, conversely, are retrieved by AERONET. On the other
525 end of the spectrum, values down to -0.5 are found in the AERONET data set when POLDER-3
526 hardly retrieves negative values. Both POLDER-3 and AERONET show a trend with the largest AOD
527 values at lower AE values. However, high AOD values (>0.9) are found with POLDER but not
528 AERONET, and are all except one associated to relatively low AE (<1). Because the cloud screening
529 of AERONET is relatively robust thanks to triplet measurements (Smirnov et al., 2000), these outliers
530 may result from undetected cloud contamination in the POLDER algorithm.

531 **4.4. Evaluation of aerosol sphericity**

532 When the geometrical conditions of observations are favourable, the coarse mode optical depth
533 (AOD_C) retrieved by POLDER-3 is quantified and apportioned into a spherical and a non-spherical
534 fraction (AOD_{CS} and AOD_{CNS} , respectively). These products are potentially very useful in
535 discriminating the mineral dust contribution, dominated by non-spherical coarse particles (e.g.,
536 Dubovik et al., 2002; Chou et al., 2008), when marine aerosols can be considered as spherical at
537 relative humidities characteristics of coastal and open-sea sites (Sayer et al., 2012a; 2012b).

538 As a prerequisite, we investigated the comparison between POLDER-derived f_{CNS} (percent fraction of
539 non-sphericity in the coarse mode AOD_C , that is, $f_{CNS} = \text{AOD}_{CNS}/(\text{AOD}_{CNS} + \text{AOD}_{CS})$) retrieved by



540 POLDER-3 and f_{NS} (percent of non-sphericity of the total AOD) estimated by AERONET. In the
541 operational ocean algorithm, f_{CNS} is a discrete value equal to 0, 0.25, 0.50, 0.75, and 1, but the
542 averaging process produces intermediate values when there is local variability between the pixels
543 around a given AERONET station

544 In general, the POLDER-3 f_{CNS} and the AERONET f_{NS} are poorly correlated. The correlation coefficient
545 R is 0.29 for the coincident data points of all the 17 stations ($N = 730$, **Table 1**). At individual stations,
546 notably the coastal and insular ones such as Lampedusa and Malaga, the correlation between
547 POLDER-3 f_{CNS} and AERONET f_{NS} is more significant ($R = 0.73$ for $N = 54$ and $R = 0.59$ for $N = 53$,
548 respectively). This is also seen when restricting the data set of Ersa and Lampedusa to the summers
549 of 2012 and 2013 ($R = 0.55$ at Ersa, $N = 11$; $R = 0.70$ at Lampedusa, $N = 10$).

550 The robustness of the comparison can be increased by further constraining the dataset to POLDER-
551 3 and AERONET AOD values larger than 0.10 and limiting the comparison to AERONET data for
552 which AOD_C is at least 30% of the total AOD. By applying these thresholds (**Figure 10**), the correlation
553 between f_{CNS} and f_{NS} is $R = 0.56$ ($N = 274$ for the 17 stations). Overall, 80% of the POLDER-3 f_{CNS}
554 agrees within 25% with the AERONET values. The largest differences occur when AERONET
555 retrieves f_{NS} values lower than 50%. In this case, only 40% of the POLDER-3 f_{CNS} are in the $\pm 25\%$
556 agreement interval with AERONET. Conversely, for AERONET $f_{NS} > 50\%$, 88% of the POLDER-3 f_{CNS}
557 agree within $\pm 25\%$ with the AERONET estimate of f_{NS} . Finally, **Figure 11** shows that a relatively good
558 agreement is obtained by comparing broad classes 25% wide, providing consistency to the
559 classification of non-sphericity by POLDER-3.

560 **5. Discussion**

561 **5.1. Evaluation of uncertainties on the advanced POLDER-3 oceanic aerosol products**

562 In this paper we provide a first comprehensive evaluation of the advanced POLDER-3 aerosol
563 products over ocean by the latest operational algorithm, based on ground-based remote sensing
564 (AERONET) but also airborne remote sensing and in situ observations (TRAQA and ADRIMED
565 campaigns) over the western Mediterranean sea. **Table 4** summarizes it by presenting the absolute



566 errors (Δ) derived from the RMS (representing the precision) and the bias (B) as a measure of
567 accuracy. For consistency with previous similar analyses and as an acknowledgment of the large size
568 of the dataset, only the RMS and the bias of the linear regressions with the AERONET data have
569 been reported. The uncertainties in AOD_{CS} and AOD_{CNS} were calculated as the square-root of the
570 quadratic sum of the errors in AOD_C and f_{CNS} .

571 Our estimate of ΔAOD indicates that, for the western Mediterranean basin, the accuracy and the
572 precision of the POLDER-3 are better than those derived by the error analysis of Tanré et al. (2011),
573 also reported in Table 4, based on a global comparison with AERONET of the POLDER-1 instrument.
574 It is noteworthy that the POLDER-1 retrieval algorithm was using a single mode spherical particle size
575 distribution (Goloub et al., 1999) instead of the current two modes allowing an aspherical component.
576 Furthermore, from our regional evaluation of the whole latest collection 3 of the POLDER-3 data set,
577 G_{frac} value for AOD (73%) is much better than that reported by Bréon et al. (2011) ($G_{frac} = 45\%$), based
578 on previous collection of POLDER-3 retrievals at a global scale.

579 **5.2. Evaluation of the fine and coarse AOD**

580 Table 4 reports the uncertainties in AOD_F and AOD_C based on estimates RMS and bias. It is
581 interesting to notice that the precision in AOD_C is apparently lower than in AOD_F (higher RMS), despite
582 the correlation being far better for the former than for the latter. We have shown that the direct
583 comparison between POLDER-3 and AERONET should take into account the differences in the
584 definition of the fine size fraction in the respective retrieval algorithms. The AERONET AOD_F is
585 recalculated from the fine mode of the volume size distribution retrieved from the measured total
586 radiance, and defined as the mode below an upper limit diameter ($D_{cut-off}$) varying between 0.88 and
587 1.98 μm . Conversely, our comparison with airborne measurements indicates that the AOD_F retrieved
588 by POLDER-3 corresponds to a fine mode extending to values of $D_{cut-off}$ between 0.6 and 0.8 μm . This
589 is expected as POLDER-3 uses polarised radiances, highly sensitive to fine particles, in agreement
590 with previous regional validations of POLDER AOD_F over land (Kacenelenbogen et al., 2006; Fan et
591 al., 2008; Wang et al., 2015). The comparison with in situ data shows that the POLDER-3 AOD_C is



592 less sensitive to the $D_{\text{cut-off}}$ value (**Figure 7**), but mostly to the extent of the coarse mode towards the
593 largest particles.

594 **5.3. Regional aerosol distribution**

595 The ability of POLDER-3 in representing the spatial distribution of aerosols in the Mediterranean
596 region is demonstrated in Figure 12 showing the retrieved products averaged over the operating
597 period. These regional maps highlights a north-south gradient for AOD and AOD_{CNS}, with, on average,
598 the highest values in the southernmost part of the western Mediterranean region, especially over
599 south Ionian Sea off Libya, as previously reported by former satellites AOD products (e.g., Moulin et
600 al., 1998; Antoine and Nobileau, 2006). The distribution of POLDER-3 AE indicates high values along
601 the European coasts (especially over the Adriatic Sea), and low along the North African coasts
602 indicative of the dominance of desert dust in the South and anthropogenic aerosol in the North of the
603 basin. AOD_F and AOD_{CS} maps show moderate spatial variability over the basin, associated to
604 averaged values (AOD_F of 0.033, AOD_{CS} of 0.021) 2 to 3 times lower than those retrieved by
605 POLDER-3 for AOD_{CNS} (0.065). Despite these low spatial patterns, it is noticeable that AOD_F values
606 tend to increase in the Eastern part of our region of study, suggesting the complexity of various aerosol
607 types influences over the Mediterranean Sea.

608 The detailed investigation of the aerosol climatology and regional distribution of the POLDER-3
609 derived aerosol optical depth load of the fine and coarse mode aerosol, including spherical and non-
610 spherical components, over the western Mediterranean Sea, as a support to the ongoing research in
611 the area, will be presented in a companion paper

612 **6. Conclusive remarks**

613 The western Mediterranean aerosol is a complex mixture with a significant temporal and spatial
614 variability at small scales (Pace et al., 2005; 2006; Di Iorio et al., 2009; Mallet et al., 2016 and
615 references therein), and significant impact on present and future regional climate (Nabat et al., 2014;
616 2015a; 2015b; 2016). High-resolved long-time series of spaceborne observations of aerosol optical
617 depth on different size classes and for differing particle shapes, such as provided by POLDER-3, are



618 essential in exploring those evolutions, directly, but also indirectly, as a term of comparison for climate
619 and transport models (Nabat et al., 2014). In the past, quantitative remote sensing of the AOD has
620 proven most useful in establishing decadal climatology of the transport of mineral dust over the basin,
621 highlighting its seasonal variability, geographic distribution and sources, link to large-scale
622 atmospheric dynamics (Dulac et al., 1992; Moulin et al., 1997a; 1997b; 1998; Antoine and Nobileau,
623 2006; Papadimas et al., 2008).

624 The quality of the observations is surely key to those surveys, and has motivated the comparative
625 analysis of the advanced POLDER-3 oceanic aerosol products during the whole period of operation
626 (March 2005 to October 2013) presented in this paper, with regards to co-located and coincident
627 ground-based measurements by AERONET, and airborne vertical profiles of aerosol optical depth
628 and size distribution during the TRAQA and ADRIMED campaign of the ChArMEx project.

629 The results presented in this paper confirm previous validations (Goloub et al., 1999; Kacenelenbogen
630 et al., 2006; Fan et al., 2008; Bréon et al., 2011; Tanré et al., 2011), and provide a first evaluation of
631 the uncertainties on the fine and coarse fractions of the aerosol optical depth, and the partitioning of
632 the coarse mode AOD into its spherical and non-spherical components. They allow moving forward
633 in the classification of the Mediterranean aerosols, and in particular in the investigation of the
634 anthropogenic fraction, which is relevant to climate change. As a matter of fact, our results indicate
635 that the fine-fraction AOD at 865 nm can be constrained to the aerosol accumulation mode below 0.6-
636 0.8 μm in diameter. This suggests that the AOD_F measured by POLDER-3 could be used for predicting
637 the submicron column concentrations for air quality studies, and for evaluating the radiative effect of
638 fine aerosols.

639 **Data availability**

640 POLDER-3 data extraction was performed with the program PARASOLASCII ([http://www-loa.univ-](http://www-loa.univ-lille1.fr/~ducoc/public/parasolascii/)
641 [lille1.fr/~ducoc/public/parasolascii/](http://www-loa.univ-lille1.fr/~ducoc/public/parasolascii/)). This version is made available from the AERIS Data and Service
642 Center (<http://www.icare.univ-lille1.fr/parasol/>). The AERONET version 2.0 aerosol products at the
643 level 2.0 quality (cloud screened and quality assured with up-to-date calibration) were obtained from
644 the official website at <http://aeronet.gsfc.nasa.gov/>. Single particle Mie scattering calculations were



645 performed with the Mie_single.pro routine under IDL available at
646 http://eodg.atm.ox.ac.uk/MIE/mie_single.html.

647 **Competing interests**

648 The authors declare that they have no conflict of interest.

649 **Special issue statement**

650 This article is part of the special issue “CHemistry and AeRosols Mediterranean Experiments
651 (ChArMEx) (ACP/AMT inter-journal SI)”. It is not associated with a conference.

652 **Acknowledgements**

653 This work is part of the ChArMEx project supported by CNRS-INSU, ADEME, Météo-France and CEA
654 in the framework of the multidisciplinary program MISTRALS (Mediterranean Integrated Studies at
655 Regional And Local Scales; <http://mistrals-home.org/>). It has also been supported by the French
656 National Research Agency (ANR) through the ADRIMED program (contract ANR-11-BS56-0006) and
657 by the French National Program of Spatial Teledetection (PNTS, <http://www.insu.cnrs.fr/pnts>, project
658 n°PNTS-2015-03). L. Mbemba Kabuiku was granted by the French Environment and Energy
659 Management Agency (ADEME) and National Center of Space Studies (CNES). Airborne data was
660 obtained using the ATR-42 atmospheric research aircraft managed by Safire, which is a joint facility
661 of the French national center for scientific research (CNRS), Météo-France and CNES. The AERIS
662 national data infrastructure provided access to the POLDER-3 data used in this study. Teams from
663 AERONET and its French component PHOTONS are acknowledged for calibrating the sun
664 photometer network and producing long-term time series of quality assured aerosol product time
665 series used in this study. We thank the AERONET principal investigators L. A. Arboledas (Alborà),
666 S. Basart and J. M. Baldasano (Barcelona), B. N. Holben (Blida), J. A. Martinez Lozano (Burjassot),
667 M. Mallet (Ersa and Montesorio Bastia), P. Goloub (Ersa), J. Piazzola (Frioul and Porquerolles), R.
668 Ellul (Gozo), D. Meloni (Lampedusa), F. J. Olmo Reyes (Malaga), S. Pignatti (Messina), J. R. Moreta
669 Gonzalez (Palma de Mallorca), G. P. Gobbi (Rome), Z. Ameur (Tizi Ouzou), S. Despiou (Toulon) and
670 D. Antoine (Villefranche-sur-Mer) and their staff for establishing and maintaining the 17 sites used in



671 this investigation. C. Di Biagio (LISA) and C. Denjean (CNRM) are acknowledged for help with data

672 analysis. G. Siour (LISA) is acknowledged for help with figure production.

673

674 **References**

- 675 Ackermann, J.: The extinction-to-backscatter ratio of tropospheric aerosol: A numerical study, *J.*
676 *Atmos. Oceanic Technol.*, 15, 1043–1050, doi:10.1175/1520-0426, 1998.
- 677 Akimoto, H.: Global air quality and pollution, *Science*, 302, 1716–1719, doi:10.1126/science.1092666,
678 2003.
- 679 Anderson, T. L., Covert, D. S., Marshall, S. F., Laucks, M. L., Charlson, R. J., Waggoner, A. P., Ogren,
680 J. a., Caldwell, R., Holm, R. L., Quant, F. R., Sem, G. J., Wiedensohler, A., Ahlquist, N. A., and
681 Bates, T. S.: Performance characteristics of a high-sensitivity, three-wavelength, total
682 scatter/backscatter nephelometer, *J. Atmos. Ocean. Technol.*, 13, 967–986, doi:10.1175/1520-
683 0426(1996)013<0967:PCOAHS>2.0.CO;2, 1996.
- 684 Anderson, T. L., and Ogren, J. A.: Determining Aerosol Radiative Properties Using the TSI 3563
685 Integrating Nephelometer, *Aerosol Sci. Technol.*, 29, 57–69, doi:10.1080/02786829808965551,
686 1998.
- 687 Antoine, D., and Nobileau, D.: Recent increase of Saharan dust transport over the Mediterranean
688 Sea, as revealed from ocean color satellite (SeaWiFS) observations, *J. Geophys. Res. Atmos.*,
689 111, 1–19, doi:10.1029/2005JD006795, 2006.
- 690 Barnaba, F. and Gobbi, G. P.: Aerosol seasonal variability over the Mediterranean region and relative
691 impact of maritime, continental and Saharan dust particles over the basin from MODIS data in
692 the year 2001, *Atmos. Chem. Phys.*, 4, 2367–2391, <https://doi.org/10.5194/acp-4-2367-2004>,
693 2004.
- 694 Becagli, S., F. Anello, C. Bommarito, F. Cassola, G. Calzolari, T. Di Iorio, A. di Sarra, J.L. Gómez-
695 Amo, F. Lucarelli, M. Marconi, D. Meloni, F. Monteleone, S. Nava, G. Pace, M. Severi, D. M.
696 Sferlazzo, R. Traversi, and Udisti R.: Constraining the ship contribution to the aerosol of the
697 central Mediterranean, *Atmos. Chem. Phys.*, 17, 2067–2084, doi: 10.5194/acp-17-2067-2017,
698 2017.
- 699 Bergametti, G., Dutot, A.-L., Buat-Ménard, P., Losno, R., and Remoudaki, E.: Seasonal variability of
700 the elemental composition of atmospheric aerosol particles over the northwestern Mediterranean,
701 *Tellus*, 41B, 353–361, doi:10.1111/j.1600-0889.1989.tb00314.x, 1989.
- 702 Bohren, C. F., and Huffman, D. R.: Absorption and scattering of light by small particles, Wiley-VCH,
703 1998.
- 704 Boucher, O.: Atmospheric aerosols Properties and Climate Impacts, 311 pp., Springer, 2015.
- 705 Boucher, O., Randall, D., Artaxo, P., Bretherton, C., Feingold, G., Forster, P., Kerminen, V.-M.,
706 Kondo, Y., Liao, H., Lohmann, U., Rasch, P., Satheesh, S. K., Sherwood, S., Stevens, B., and
707 Zhang, X. Y.: Clouds and Aerosols, in *Climate Change 2013 - The Physical Science Basis*, edited
708 by Intergovernmental Panel on Climate Change, pp. 571–658, Cambridge University Press,
709 Cambridge., 2013.
- 710 Bréon, F.-M., and Colzy, S.: Cloud detection from the spaceborne POLDER instrument and validation
711 against surface synoptic observations, *J. Appl. Meteorol.*, 38, 777–785, doi:10.1175/1520-
712 0450(1999)038<0777:CDFSTP>2.0.CO;2, 1999.
- 713 Bréon, F. M., Vermeulen, A., and Descloitres, J.: An evaluation of satellite aerosol products against
714 sunphotometer measurements, *Remote Sens. Environ.*, 115, 3102–3111,
715 doi:10.1016/j.rse.2011.06.017, 2011.
- 716 Cai, Y., Montague, D. C., Mooiweer-Bryan, W., and Deshler, T.: Performance characteristics of the
717 ultra high sensitivity aerosol spectrometer for particles between 55 and 800 nm: Laboratory and
718 field studies, *J. Aerosol Sci.*, 39, 759–769, doi:10.1016/j.jaerosci.2008.04.007, 2008.
- 719 Chou, C., Formenti, P., Maille, M., Ausset, P., Helas, G., Harrison, M, and Osborne, S.: Size
720 distribution, shape, and composition of mineral dust aerosols collected during the African
721 Monsoon Multidisciplinary Analysis Special Observation Period 0: Dust and Biomass-Burning
722 Experiment field campaign in Niger, January 2006, *J. Geophys. Res. Atmos.*, 113, 1–17,
723 doi:10.1029/2008JD009897, 2008.
- 724 Christensen, J. H., Kumar, K. K., Aldria, E., An, S.-I., Cavalcanti, I. F. a., Castro, M. De, Dong, W.,
725 Goswami, P., Hall, A., Kanyanga, J. K., Kitoh, A., Kossin, J., Lau, N.-C., Renwick, J., Stephenson,
726 D. B., Xie, S.-P. and Zhou, T.: Climate Phenomena and their Relevance for Future Regional
727 Climate Change, in *Climate Change 2013 - The Physical Science Basis*, edited by



- 728 Intergovernmental Panel on Climate Change, pp. 1217–1308, Cambridge University Press,
729 Cambridge., 2013.
- 730 Cros, B., Durand, P., Cachier, H., Drobinski, P., Fréjafon, E., Kottmeier, C., Perros, P. E., Peuch, V.
731 H., Ponche, J. L., Robin, D., Saïd, F., Toupance, G., and Wortham, H.: The ESCOMPTE program:
732 An overview, *Atmos. Res.*, 69, 241–279, doi:10.1016/j.atmosres.2003.05.001, 2004.
- 733 Denjean C., Cassola F., Mazzino A., Triquet S., Chevaillier S., Grand N., Bourriante T., Momboisse
734 G., Sellegri K., Schwarzenbock A., Freney E., Mallet M., and Formenti P., Size distribution and
735 optical properties of mineral dust aerosols transported in the western Mediterranean, *Atmos.*
736 *Chem. Phys.*, 16, 1081–1104, doi:10.5194/acp-16-1081-2016, 2016.
- 737 Deuzé, J. L., Herman, M., Goloub, P., Tanré, D., and Marchand, A.: Characterization of aerosols over
738 ocean from POLDER/ADEOS-1, *Geophys. Res. Lett.*, 26, 1421, doi:10.1029/1999GL900168,
739 1999.
- 740 Deuzé, J. L., Goloub, P., Herman, M., Marchand, A., Perry, G., Susana, S., and Tanré, D.: Estimate
741 of the aerosol properties over the ocean with POLDER, *J. Geophys. Res. Atmos.*, 105, 15329–
742 15346, doi:10.1029/2000JD900148, 2000.
- 743 Di Biagio, C., Doppler, L., Gaimoz, C., Grand, N., Ancellet, G., Raut, J.-C., Beekmann, M., Borbon,
744 A., Sartelet, K., Attié, J.-L., Ravetta, F., and Formenti, P.: Continental pollution in the western
745 Mediterranean basin: vertical profiles of aerosol and trace gases measured over the sea during
746 TRAQA 2012 and SAFMED 2013, *Atmos. Chem. Phys.*, 15, 9611–9630, doi:10.5194/acp-15-
747 9611-2015, 2015.
- 748 Di Biagio C., Formenti P., Doppler L., Gaimoz C., Grand N., Ancellet G., Attié J.L., Bucci S., Dubuisson
749 P., Fierli F., Mallet M., and Ravetta F., Continental pollution in the Western Mediterranean basin:
750 large variability of the aerosol single scattering albedo and influence on the direct shortwave
751 radiative effect, *Atmos. Chem. Phys.*, 16, 10591–10607, doi:10.5194/acp-16-10591-2016, 2016.
- 752 Di Iorio, T., di Sarra, A., Sferlazzo, D. M., Cacciani, M., Meloni, D., Monteleone, F., Fuà, D., and
753 Fiocco, G.: Seasonal evolution of the tropospheric aerosol vertical profile in the central
754 Mediterranean and role of desert dust, *J. Geophys. Res.*, 114, D02201,
755 doi:10.1029/2008jd010593, 2009.
- 756 Di Sarra, A., Pace, G., Meloni, D., De Silvestri, L., Piacentino, S., and Monteleone, F.: Surface
757 shortwave radiative forcing of different aerosol types in the central Mediterranean, *Geophys. Res.*
758 *Lett.*, 35, L02714, doi:10.1029/2007GL032395, 2008.
- 759 Dubovik, O., and King, M. D.: A flexible inversion algorithm for retrieval of aerosol optical properties
760 from Sun and sky radiance measurements, *J. Geophys. Res. Atmos.*, 105, 20673–20696,
761 doi:10.1029/2000JD900282, 2000.
- 762 Dubovik, O., Holben, B., Eck, T. F., Smirnov, A., Kaufman, Y. J., King, M. D., Tanré, D., and Slutsker,
763 I.: Variability of Absorption and Optical Properties of Key Aerosol Types Observed in Worldwide
764 Locations, *J. Atmos. Sci.*, 59, 590–608, doi:10.1175/1520-0469(2002);2, 2002.
- 765 Dubovik, O., Sinyuk, A., Lapyonok, T., Holben, B. N., Mishchenko, M., Yang, P., Eck, T. F., Volten,
766 H., Muñoz, O., Veihelmann, B., van der Zande, W. J., Leon, J.-F., Sorokin, M., and Slutsker, I.:
767 Application of spheroid models to account for aerosol particle nonsphericity in remote sensing of
768 desert dust, *J. Geophys. Res.*, 111, D11208, doi:10.1029/2005JD006619, 2006.
- 769 Dulac, F., and Chazette, P.: Airborne study of a multi-layer aerosol structure in the eastern
770 Mediterranean observed with the airborne polarized lidar ALEX during a STAAARTE campaign
771 (7 June 1997), *Atmos. Chem. Phys.*, 3, 1817–1831, doi:10.5194/acp-3-1817-2003, 2003.
- 772 Dulac, F., Tanré, D., Bergametti, G., Buat-Ménard, P., Desbois, M., and Sutton, D.: Assessment of
773 the African airborne dust mass over the western Mediterranean Sea using Meteosat data, *J.*
774 *Geophys. Res.*, 97, 2489, doi:10.1029/91JD02427, 1992.
- 775 Fan, X., Goloub, P., Deuzé, J. L., Chen, H., Zhang, W., Tanré, D., and Li, Z.: Evaluation of PARASOL
776 aerosol retrieval over North East Asia, *Remote Sens. Environ.*, 112, 697–707,
777 doi:10.1016/j.rse.2007.06.010, 2008.
- 778 Formenti, P., Boucher, O., Reiner, T., Sprung, D., Andreae, M. O., Wendisch, M., Wex, H., Kindred,
779 D., Tzortziou, M., Vasaras, A., and Zerefos, C.: STAAARTE-MED 1998 summer airborne
780 measurements over the Aegean Sea 2. Aerosol scattering and absorption, and radiative
781 calculations, *J. Geophys. Res. Atmos.*, 107, doi:10.1029/2001JD001536, 2002.



- 782 Formenti, P., Rajot, J. L., Desboeufs, K., Saïd, F., Grand, N., Chevallier, S., and Schmechtig, C.:
783 Airborne observations of mineral dust over western Africa in the summer Monsoon season:
784 spatial and vertical variability of physico-chemical and optical properties, *Atmos. Chem. Phys.*,
785 11, 6387–6410, doi:10.5194/acp-11-6387-2011, 2011.
- 786 García-Ruiz, J. M., López-Moreno, J. I., Vicente-Serrano, S. M., Lasanta-Martínez, T., and Beguería,
787 S.: Mediterranean water resources in a global change scenario, *Earth-Science Rev.*, 105, 121–
788 139, doi:10.1016/j.earscirev.2011.01.006, 2011.
- 789 Giorgi, F.: Climate change hot-spots, *Geophys. Res. Lett.*, 33, L08707, doi:10.1029/2006GL025734,
790 2006.
- 791 Giorgi, F., and Lionello, P.: Climate change projections for the Mediterranean region, *Glob. Planet.*
792 *Change*, 63, 90–104, doi:10.1016/j.gloplacha.2007.09.005, 2008.
- 793 Gkikas, A., Hatzianastassiou, N., and Mihalopoulos, N.: Aerosol events in the broader Mediterranean
794 basin based on 7-year (2000–2007) MODIS C005 data, *Ann. Geophys.*, 27, 3509–3522,
795 doi:10.5194/angeo-27-3509-2009, 2009.
- 796 Gkikas, A., Basart, S., Hatzianastassiou, N., Marinou, E., Amiridis, V., Kazadzis, S., Pey, J., Querol,
797 X., Jorba, O., Gassó, S., and Baldasano, J. M.: Mediterranean intense desert dust outbreaks and
798 their vertical structure based on remote sensing data, *Atmos. Chem. Phys.*, 16, 8609–8642,
799 doi:10.5194/acp-16-8609-2016, 2016.
- 800 Goloub, P., Tanré, D., Deuzé, J. L., Herman, M., Marchand, A., and Bréon, F.-M.: Validation of the
801 first algorithm applied for deriving the aerosol properties over the ocean using the
802 POLDER/ADEOS measurements, *IEEE Trans. Geosci. Remote Sens.*, 37, 1586–1596,
803 doi:10.1109/36.763270, 1999.
- 804 Granados-Muñoz, M. J., Navas-Guzmán, F., Luis Guerrero-Rascado, J., Antonio Bravo-Aranda, J.,
805 Biniotoglou, I., Nepomuceno Pereira, S., Basart, S., Baldasano, J. M., Belegante, L., Chaikovsky,
806 A., Comerón, A., D'Amico, G., Dubovik, O., Ilic, L., Kokkalis, P., Muñoz-Porcar, C., Nickovic, S.,
807 Nicolae, D., José Olmo, F., Papayannis, A., Pappalardo, G., Rodríguez, A., Schepanski, K.,
808 Sicard, M., Vukovic, A., Wandinger, U., Dulac, F., and Alados-Arboledas, L.: Profiling of aerosol
809 microphysical properties at several EARLINET/AERONET sites during the July 2012
810 ChArMEx/EMEP campaign, *Atmos. Chem. Phys.*, 16, 7043–7066, doi:10.5194/acp-16-7043-
811 2016, 2016.
- 812 Grimm, H., and Eatough, D. J.: Aerosol measurement: the use of optical light scattering for the
813 determination of particulate size distribution, and particulate mass, including the semi-volatile
814 fraction., *J. Air Waste Manag. Assoc.*, 59, 101–107, doi:10.3155/1047-3289.59.1.101, 2009.
- 815 Herman, M., Deuzé, J. L., Marchand, A., Roger, B., and Lallart, P.: Aerosol remote sensing from
816 POLDER/ADEOS over the ocean: Improved retrieval using a nonspherical particle model, *J.*
817 *Geophys. Res.*, 110, D10S02, doi:10.1029/2004JD004798, 2005.
- 818 Holben, B. N., Eck, T. F., Slutsker, I., Tanré, D., Buis, J. P., Setzer, A., Vermote, E., Reagan, J. A.,
819 Kaufman, Y. J., Nakajima, T., Lavenu, F., Jankowiak, I., and Smirnov, A.: AERONET - A
820 federated instrument network and data archive for aerosol characterization, *Remote Sens.*
821 *Environ.*, 66, 1–16, doi:10.1016/S0034-4257(98)00031-5, 1998.
- 822 Holben, B. N., Tanré, D., Smirnov, A., Eck, T. F., Slutsker, I., Abuhassan, N., Newcomb, W. W.,
823 Schafer, J. S., Chatenet, B., Lavenu, F., Kaufman, Y. J., Castle, J. Vande, Setzer, A., Markham,
824 B., Clark, D., Frouin, R., Halthore, R., Karneli, A., O'Neill, N. T., Pietras, C., Pinker, R. T., Voss,
825 K., and Zibordi, G.: An emerging ground-based aerosol climatology: Aerosol optical depth from
826 AERONET, *J. Geophys. Res. Atmos.*, 106, 12067–12097, doi:10.1029/2001JD900014, 2001.
- 827 Kacenelenbogen, M., Léon, J.-F., Chiapello, I., and Tanré, D.: Characterization of aerosol pollution
828 events in France using ground-based and POLDER-2 satellite data, *Atmos. Chem. Phys.*, 6,
829 4851–4866, 2006.
- 830 Kalivitis, N., Bougiatioti, A., Kouvarakis, G., and Mihalopoulos, N.: Long term measurements of
831 atmospheric aerosol optical properties in the Eastern Mediterranean, *Atmos. Res.*, 102, 351–
832 357, doi:10.1016/j.atmosres.2011.08.013, 2011.
- 833 Karol, Y., Tanré, D., Goloub, P., Vervaerde, C., Balois, J. Y., Blarel, L., Podvin, T., Mortier, A., and
834 Chaikovsky, A.: Airborne sun photometer PLASMA: concept, measurements, comparison of
835 aerosol extinction vertical profile with lidar, *Atmos. Meas. Tech.*, 6, 2383–2389, doi:10.5194/amt-
836 6-2383-2013, 2013.



- 837 Kebabian, P. L., Robinson, W. A., and Freedman, A.: Optical extinction monitor using cw cavity
838 enhanced detection, *Rev. Sci. Instrum.*, 78, doi:10.1063/1.2744223, 2007.
- 839 Kim, D., Chin, M., Yu, H., Diehl, T., Tan, Q., Kahn, R. A., Tsigaridis, K., Bauer, S. E., Takemura, T.,
840 Pozzoli, L., Bellouin, N., Schulz, M., Peyridieu, S., Chédin, A., and Koffi, B.: Sources, sinks, and
841 transatlantic transport of North African dust aerosol: A multimodel analysis and comparison with
842 remote sensing data, *J. Geophys. Res. Atmos.*, 119, 6259–6277, doi:10.1002/2013JD021099,
843 2014.
- 844 Kovats, R. S., Valentini, R., Bouwer, L. M., Georgopoulou, E., Jacob, D., Martin, E., Rounsevell, M.,
845 and Soussana, J.-F.: Europe, in *Climate Change 2014: Impacts, Adaptation, and Vulnerability*.
846 Part B: Regional Aspects, Contribution of Working Group II to Fifth Assessment Report of the
847 Intergovernmental Panel on Climate Change, Eds. Barros, V.R., Field, C.B., Dokken, D.J.,
848 Mastrandrea, M.D., Mach, K.J., Bilir, T.E., Chatterjee, M., Ebi, K.L., Estrada, Y.O., Genova, R.C.,
849 Girma, B., Kissel, E.S., Levy, A.N., MacCracken, S., Mastrandrea, P.R., and White, L.L.,
850 Cambridge University Press, 1267–1326, 2014.
- 851 Kubilay, N., Cokacar, T., and Oguz, T.: Optical properties of mineral dust outbreaks over the
852 northeastern Mediterranean, *J. Geophys. Res. Atmos.*, 108, 1–10, doi:10.1029/2003JD003798,
853 2003.
- 854 Lelieveld, J., Berresheim, H., Borrmann, S., Crutzen, P. J., Dentener, F. J., Fischer, H., Feichter, J.,
855 Flatau, P. J., Heland, J., Holzinger, R., Korrmann, R., Lawrence, M. G., Levin, Z., Markowicz, K.
856 M., Mihalopoulos, N., Minikin, a, Ramanathan, V., De Reus, M., Roelofs, G. J., Scheeren, H. a,
857 Sciare, J., Schlager, H., Schultz, M., Siegmund, P., Steil, B., Stephanou, E. G., Stier, P., Traub,
858 M., Warneke, C., Williams, J., and Ziereis, H.: Global air pollution crossroads over the
859 Mediterranean, *Science*, 298, 794–9, doi:10.1126/science.1075457, 2002.
- 860 Liu, P. S. K., Leaitch, W. R., Strapp, J. W., and Wasey, M. A.: Response of Particle Measuring
861 Systems Airborne ASAP and PCASP to NaCl and Latex Particles, *Aerosol Sci. Technol.*, 16,
862 83–95, doi:10.1080/02786829208959539, 1992.
- 863 Lyamani, H., Valenzuela, A., Perez-Ramirez, D., Toledano, C., Granados-Muñoz, M. J., Olmo, F. J.,
864 and Alados-Arboledas, L.: Aerosol properties over the western Mediterranean basin: temporal
865 and spatial variability, *Atmos. Chem. Phys.*, 15, 2473–2486, doi:10.5194/acp-15-2473-2015,
866 2015.
- 867 Mallet, M., Dubovik, O., Nabat, P., Dulac, F., Kahn, R., Sciare, J., Paronis, D. and Léon, J. F.:
868 Absorption properties of Mediterranean aerosols obtained from multi-year ground-based remote
869 sensing observations, *Atmos. Chem. Phys.*, 13, 9195–9210, doi:10.5194/acp-13-9195-2013,
870 2013.
- 871 Mallet, M., Dulac, F., Formenti, P., Nabat, P., Sciare, J., Roberts, G., Pelon, J., Ancellet, G., Tanré,
872 D., Parol, F., Denjean, C., Brogniez, G., di Sarra, A., Alados-Arboledas, L., Arndt, J., Auriol, F.,
873 Blarel, L., Bourriane, T., Chazette, P., Chevaillier, S., Claeys, M., D'Anna, B., Derimian,
874 Y., Desboeufs, K., Di Iorio, T., Doussin, J.-F., Durand, P., Féron, A., Freney, E., Gaimoz, C.,
875 Goloub, P., Gómez-Amo, J. L., Granados-Muñoz, M. J., Grand, N., Hamonou, E., Jankowiak, I.,
876 Jeannot, M., Léon, J.-F., Maillé, M., Mailler, S., Meloni, D., Menut, L., Momboisse, G., Nicolas,
877 J., Podvin, T., Pont, V., Rea, G., Renard, J.-B., Roblou, L., Schepanski, K., Schwarzenboeck, A.,
878 Sellegri, K., Sicard, M., Solmon, F., Somot, S., Torres, B., Totems, J., Triquet, S., Verdier, N.,
879 Verwaerde, C., Waquet, F., Wenger, J., and Zapf, P.: Overview of the Chemistry-Aerosol
880 Mediterranean Experiment/Aerosol Direct Radiative Forcing on the Mediterranean Climate
881 (ChArMEX/ADRIMED) summer 2013 campaign, *Atmos. Chem. Phys.*, 16, 455–504,
882 doi:10.5194/acp-16-455-2016, 2016.
- 883 Markwardt, C. B.: Non-linear least squares fitting in IDL with MPFIT, in *Proc. Astronomical Data*
884 *Analysis Software and Systems XVIII*, eds. D. Bohlender, P. Dowler & D. Durand, *Astron. Soc.*
885 *Pac. Conf. Ser.*, 411, 251, 2009.
- 886 Massoli, P., Kebabian, P. L., Onasch, T. B., Hills, F. B. and Freedman, A.: Aerosol light extinction
887 measurements by Cavity Attenuated Phase Shift (CAPS) spectroscopy: Laboratory validation
888 and field deployment of a compact aerosol particle extinction monitor, *Aerosol Sci. Technol.*,
889 44(6), 428–435, doi:10.1080/02786821003716599, 2010.
- 890 Meloni, D., di Sarra, A., Biavati, G., Deuisi, J.J., Monteleone, F., Pace, G., Piacentino, S., and
891 Sferlazzo, D. M. : Seasonal behavior of Saharan dust events at the Mediterranean island of



- 892 Lampedusa in the period 1999–2005, *Atmos. Environ.*, 41, 3041–3056,
893 doi:10.1016/j.atmosenv.2006.12.001, 2007.
- 894 Mie, G.: Beiträge zur Optik trüber Medien, speziell kolloidaler Metallösungen, *Ann. Phys.*, 330, 377–
895 445, doi:10.1002/andp.19083300302, 1908.
- 896 Migon, C., Alleman, L., Leblond, N., and Nicolas, E.: Evolution of atmospheric lead over the
897 northwestern Mediterranean between 1986 and 1992, *Atmos Environ.A.*, 27, 2161–2167,
898 doi:10.1016/0960-1686(93)90045-Z, 1993.
- 899 Mihalopoulos, N., Stephanou, E., Kanakidou, M., Pilitsidis, S., and Bousquet, P.: Tropospheric
900 aerosol ionic composition in the Eastern Mediterranean region. *Tellus B*, 49, 314–326.
901 doi:10.1034/j.1600-0889.49.issue3.7.x, 1997.
- 902 Mishchenko, M. I., Travis, L. D., Kahn, R. A., and West, R. A.: Modeling phase function for dustlike
903 tropospheric aerosols using a shape mixture of randomly oriented polydisperse spheroids, *J.*
904 *Geophys. Res.*, 102, 16831–16847, doi:10.1029/96JD02110, 1997.
- 905 Monks, P. S., Granier, C., Fuzzi, S., Stohl, A., Williams, M. L., Akimoto, H., Amann, M., Baklanov, A.,
906 Baltensperger, U., Bey, I., Blake, N., Blake, R. S., Carslaw, K., Cooper, O. R., Dentener, F.,
907 Fowler, D., Fragkou, E., Frost, G. J., Generoso, S., Ginoux, P., Grewe, V., Guenther, A.,
908 Hansson, H. C., Henne, S., Hjorth, J., Hofzumahaus, A., Huntrieser, H., Isaksen, I. S. A., Jenkin,
909 M. E., Kaiser, J., Kanakidou, M., Klimont, Z., Kulmala, M., Laj, P., Lawrence, M. G., Lee, J. D.,
910 Liousse, C., Maione, M., McFiggans, G., Metzger, A., Mieville, A., Moussiopoulos, N., Orlando,
911 J. J., O'Dowd, C. D., Palmer, P. I., Parrish, D. D., Petzold, A., Platt, U., Pöschl, U., Prévôt, A. S.
912 H., Reeves, C. E., Reimann, S., Rudich, Y., Sellegri, K., Steinbrecher, R., Simpson, D., ten Brink,
913 H., Theloke, J., van der Werf, G. R., Vautard, R., Vestreng, V., Vlachokostas, C., and von Glasow,
914 R.: Atmospheric composition change – global and regional air quality, *Atmos. Environ.*, 43, 5268–
915 5350, doi:10.1016/j.atmosenv.2009.08.021, 2009.
- 916 Moulin, C., Guillard, F., Dulac, F., and Lambert, C. E.: Long-term daily monitoring of Saharan dust
917 load over ocean using Meteosat ISCCP-B2 data: 1. Methodology and preliminary results for
918 1983–1994 in the Mediterranean, *J. Geophys. Res.*, 102, 16947, doi:10.1029/96JD02620, 1997a.
- 919 Moulin, C., Lambert, C. E., Dulac, F., and Dayan, U.: Control of atmospheric export of dust from North
920 Africa by the North Atlantic Oscillation, *Nature*, 387 (6634), 691–694, 1997b.
- 921 Moulin, C., Lambert, C. E., Dayan, U., Masson, V., Ramonet, M., Bousquet, P., Legrand, M.,
922 Balkanski, Y. J., Guelle, W., Marticorena, B., Bergametti, G., and Dulac, F.: Satellite climatology
923 of African dust transport in the Mediterranean atmosphere, *J. Geophys. Res.*, 103, 13137,
924 doi:10.1029/98JD00171, 1998.
- 925 Müller, T., Nowak, A., Wiedensohler, A., Sheridan, P., Laborde, M., Covert, D. S., Marinoni, A., Imre,
926 K., Henzing, B., Roger, J.-C., Martins dos Santos, S., Wilhelm, R., Wang, Y.-Q. and de Leeuw,
927 G.: Angular illumination and truncation of three different integrating nephelometers: Implications
928 for empirical, size-based corrections, *Aerosol Sci. Technol.*, 43, 581–586,
929 doi:10.1080/02786820902798484, 2009.
- 930 Myhre, G., Shindell, D., Bréon, F.-M., Collins, W., Fuglestedt, J., Huang, J., Koch, D., Lamarque, J.-
931 F., Lee, D., Mendoza, B., Nakajima, T., Robock, A., Stephens, G., Takemura, T., and Zhan, H.:
932 Anthropogenic and Natural Radiative Forcing, in *Climate Change 2013: The Physical Science*
933 *Basis*, pp. 659–740, 2013.
- 934 Nabat, P., Somot, S., Mallet, M., Chiapello, I., Morcrette, J. J., Solmon, F., Szopa, S., Dulac, F.,
935 Collins, W., Ghan, S., Horowitz, L. W., Lamarque, J. F., Lee, Y. H., Naik, V., Nagashima, T.,
936 Shindell, D., and Skeie, R.: A 4-D climatology (1979–2009) of the monthly tropospheric aerosol
937 optical depth distribution over the Mediterranean region from a comparative evaluation and
938 blending of remote sensing and model products, *Atmos. Meas. Tech.*, 6, 1287–1314,
939 doi:10.5194/amt-6-1287-2013, 2013.
- 940 Nabat, P., Somot, S., Mallet, M., Sanchez-Lorenzo, A., and Wild, M.: Contribution of anthropogenic
941 sulfate aerosols to the changing Euro-Mediterranean climate since 1980, *Geophys. Res. Lett.*,
942 41, doi:10.1002/2014GL060798, 2014.
- 943 Nabat, P., Somot, S., Mallet, M., Michou, M., Sevault, F., Driouech, F., Meloni, D., di Sarra, A., Di
944 Biagio, C., Formenti, P., Sicard, M., Léon, J.-F., and Bouin, M.-N.: Dust aerosol radiative effects
945 during summer 2012 simulated with a coupled regional aerosol–atmosphere–ocean model over
946 the Mediterranean, *Atmos. Chem. Phys.*, 15, 3303–3326, doi:10.5194/acp-15-3303-2015, 2015a.



- 947 Nabat P., S. Somot, M. Mallet, F. Sevault, M. Chiacchio, and M. Wild: Direct and semi-direct aerosol
948 radiative effect on the Mediterranean climate variability using a coupled regional climate system
949 model, *Clim. Dyn.*, 44, 1127-1155, doi:10.1007/s00382-014-2205-6, 2015b.
- 950 Nabat, P., Kiki, Somot, S., Mallet, M. and Michou, M.: Impact of aerosols in regional climate
951 projections over the Mediterranean area, in *Air Pollution Modeling and its Application XXIV*,
952 Springer, Ed. by Steyn, D. G., and Chaumerliac, N., pp. 73-78, doi:10.1007/978-3-319-24478-
953 5_12, 2016.
- 954 Pace, G., Meloni, D., and di Sarra, A.: Forest fire aerosol over the Mediterranean basin during summer
955 2003, *J. Geophys. Res.*, 110, D21202, doi:10.1029/2005jd005986, 2005.
- 956 Pace, G., di Sarra, A., Meloni, D., Piacentino, S., and Chamard, P.: Aerosol optical properties at
957 Lampedusa (Central Mediterranean). 1. Influence of transport and identification of different
958 aerosol types, *Atmos. Chem. Phys.*, 6, 697–713, doi:10.5194/acp-6-697-2006, 2006.
- 959 Pan, X., Chin, M., Gautam, R., Bian, H., Kim, D., Colarco, P. R., Diehl, T. L., Takemura, T., Pozzoli,
960 L., Tsigaridis, K., Bauer, S. and Bellouin, N.: A multi-model evaluation of aerosols over South
961 Asia: Common problems and possible causes, *Atmos. Chem. Phys.*, 15(10), 5903–5928,
962 doi:10.5194/acp-15-5903-2015, 2015.
- 963 Papadimas, C. D., Hatzianastassiou, N., Mihalopoulos, N., Querol, X., and Vardavas, I.: Spatial and
964 temporal variability in aerosol properties over the Mediterranean basin based on 6-year (2000–
965 2006) MODIS data, *J. Geophys. Res.*, 113, D11205, doi:10.1029/2007JD009189, 2008.
- 966 Pappalardo, G., Amodeo, A., Apituley, A., Comeron, A., Freudenthaler, V., Linné, H., Ansmann, A.,
967 Bösenberg, J., D'Amico, G., Mattis, I., Mona, L., Wandinger, U., Amiridis, V., Alados-Arboledas,
968 L., Nicolae, D., and Wiegner, M.: EARLINET: Towards an advanced sustainable European
969 aerosol lidar network, *Atmos. Meas. Tech.*, 7, 2389–2409, doi:10.5194/amt-7-2389-2014, 2014.
- 970 Pérez, N., Pey, J., Castillo, S., Viana, M., Alastuey, A., and Querol, X.: Interpretation of the variability
971 of levels of regional background aerosols in the Western Mediterranean, *Sci. Total Environ.*, 407,
972 527-540, doi:10.1016/j.scitotenv.2008.09.006, 2008.
- 973 Petzold, A., Rasp, K., Weinzierl, B., Esselborn, M., Hamburger, T., Dörnbrack, A., Kandler, K., Schütz,
974 L., Knippertz, P., Fiebig, M., and Virkkula, A.: Saharan dust absorption and refractive index from
975 aircraft-based observations during SAMUM 2006, *Tellus B*, 61, 118-130, 10.1111/j.1600-
976 0889.2008.00383.x, 2009.
- 977 Petzold, A., Onasch, T., Kebejian, P., and Freedman, A.: Intercomparison of a Cavity Attenuated
978 Phase Shift-based extinction monitor (CAPS PMex) with an integrating nephelometer and a filter-
979 based absorption monitor, *Atmos. Meas. Tech.*, 6, 1141–1151, doi:10.5194/amt-6-1141-2013,
980 2013.
- 981 Pey, J., Querol, X., Alastuey, A., Forastiere, F. and Stafoggia, M.: African dust outbreaks over the
982 Mediterranean Basin during 2001-2011: PM10 concentrations, phenomenology and trends, and
983 its relation with synoptic and mesoscale meteorology, *Atmos. Chem. Phys.*, 13, 1395–1410,
984 doi:10.5194/acp-13-1395-2013, 2013.
- 985 Pope III, C. A., Burnett, R. T., Thun, M. J., Calle, E. E., Krewski, D., Ito, K., and Thurston, G. D.: Lung
986 Cancer, Cardiopulmonary Mortality, and Long-term Exposure to Fine Particulate Air Pollution, *J.*
987 *AMA*, 287, 1132, doi:10.1001/jama.287.9.1132, 2002.
- 988 Pope III, C. A., and Dockery, D. W.: Health Effects of Fine Particulate Air Pollution: Lines that Connect,
989 *J. Air Waste Manage. Assoc.*, 56, 709–742, doi:10.1080/10473289.2006.10464485, 2006.
- 990 Putaud, J.-P., Van Dingenen, R., Dell'Acqua, A., Raes, F., Matta, E., Decesari, S., Facchini, M. C., and
991 Fuzzi, S.: Size-segregated aerosol mass closure and chemical composition in Monte Cimone (I)
992 during MINATROC, *Atmos. Chem. Phys.*, 4, 889–902, doi:10.5194/acp-4-889-2004, 2004.
- 993 Querol, X., Alastuey, A., Pey, J., Cusack, M., Pérez, N., Mihalopoulos, N., Theodosi, C.,
994 Gerasopoulos, E., Kubilay, N., and Koçak, M.: Variability in regional background aerosols within
995 the Mediterranean, *Atmos. Chem. Phys.*, 9, 4575–4591, doi:10.5194/acp-9-4575-2009, 2009.
- 996 Rea G., Turquety S., Menuet L., Briant R., Mailler S., and Siour G.: Source contributions to 2012
997 summertime aerosols in the Euro-Mediterranean region, *Atmos. Chem. Phys.*, 15, 8013–8036,
998 doi:10.5194/acp-15-8013-2015, 2015.
- 999 Reid, J. S., Eck, T. F., Christopher, S. a., Hobbs, P. V., and Holben, B.: Use of the Ångström exponent
1000 to estimate the variability of optical and physical properties of aging smoke particles in Brazil, *J.*
1001 *Geophys. Res. Atmos.*, 104, 27473–27489, doi:10.1029/1999JD900833, 1999.



- 1002 Reid, J. S., Kinney, J. E., Westphal, D. L., Holben, B. N., Welton, E. J., Tsay, S.-C., Eleuterio, D. P.,
1003 Campbell, J. R., Christopher, S. A., Colarco, P. R., Jonsson, H. H., Livingston, J. M., Maring, H.
1004 B., Meier, M. L., Pilewskie, P., Prospero, J. M., Reid, E. A., Remer, L. A., Russell, P. B., Savoie,
1005 D. L., Smirnov, A., and Tanré, D.: Analysis of measurements of Saharan dust by airborne and
1006 ground-based remote sensing methods during the Puerto Rico Dust Experiment (PRIDE), *J.*
1007 *Geophys. Res.*, 108, 8586, doi:10.1029/2002JD002493, 2003.
- 1008 Ryder, C. L., Highwood, E. J., Rosenberg, P. D., Trembath, J., Brooke, J. K., Bart, M., Dean, A.,
1009 Crosier, J., Dorsey, J., Brindley, H., Banks, J., Marsham, J. H., McQuaid, J. B., Sodemann, H.,
1010 and Washington, R.: Optical properties of Saharan dust aerosol and contribution from the coarse
1011 mode as measured during the Fennec 2011 aircraft campaign, *Atmos. Chem. Phys.*, 13, 303–
1012 325, doi:10.5194/acp-13-303-2013, 2013.
- 1013 Sayer, A. M., Smirnov, A., Hsu, N. C., Munchak, L. A., and Holben, B. N.: Estimating marine aerosol
1014 particle volume and number from Maritime Aerosol Network data, *Atmos. Chem. Phys.*, 12, 8889–
1015 8909, doi:10.5194/acp-12-8889-2012, 2012a.
- 1016 Sayer, A. M., Hsu, N. C., Bettenhausen, C., Ahmad, Z., Holben, B. N., Smirnov, A., Thomas, G. E.,
1017 and Zhang, J.: SeaWiFS Ocean Aerosol Retrieval (SOAR): Algorithm, validation, and comparison
1018 with other data sets, *J. Geophys. Res. Atmos.*, 117, 1–17, doi:10.1029/2011JD016599, 2012b.
- 1019 Shindell, D. T., Lamarque, J. F., Schulz, M., Flanner, M., Jiao, C., Chin, M., Young, P. J., Lee, Y. H.,
1020 Rotstain, L., Mahowald, N., Milly, G., Faluvegi, G., Balkanski, Y., Collins, W. J., Conley, A. J.,
1021 Dalsoren, S., Easter, R., Ghan, S., Horowitz, L., Liu, X., Myhre, G., Nagashima, T., Naik, V.,
1022 Rumbold, S. T., Skeie, R., Sudo, K., Szopa, S., Takemura, T., Voulgarakis, A., Yoon, J. H., and
1023 Lo, F.: Radiative forcing in the ACCMIP historical and future climate simulations, *Atmos. Chem.*
1024 *Phys.*, 13, 2939–2974, doi:10.5194/acp-13-2939-2013, 2013.
- 1025 Sicard, M., Barragan, R., Muñoz-Porcar, C., Comerón, A., Mallet, M., Dulac, F., Pelon, J., Alados
1026 Arboledas, L., Amodeo, A., Boselli, A., Bravo-Aranda, J. A., D'amico, G., Granados Muñoz, M.
1027 J., Leto, G., Guerrero Rascado, J. L., Madonna, F., Mona, L., Pappalardo, G., Perrone, M. R.,
1028 Burlizzi, P., Rocadenbosch, F., Rodríguez-Gómez, A., Scollo, S., Spinelli, N., Titos, G., Wang,
1029 X., and Zanmar Sanchez, R.: Contribution of EARLINET/ACTRIS to the summer 2013 Special
1030 Observing Period of the ChArMEx project: monitoring of a Saharan dust event over the western
1031 and central Mediterranean, *Int. J. Remote Sens.*, 37, 4698–4711,
1032 doi:10.1080/01431161.2016.1222102, 2016.
- 1033 Smirnov, A., Holben, B. N., Eck, T. F., Dubovik, O., and Slutsker, I.: Cloud-screening and quality
1034 control algorithms for the AERONET database, *Remote Sens. Environ.*, 73, 337–349,
1035 doi:10.1016/S0034-4257(00)00109-7, 2000.
- 1036 Smirnov, A., Holben, B. N., Giles, D. M., Slutsker, I., O'Neill, N. T., Eck, T. F., Macke, A., Croot, P.,
1037 Courcoux, Y., Sakerin, S. M., Smyth, T. J., Zielinski, T., Zibordi, G., Goes, J. I., Harvey, M. J.,
1038 Quinn, P. K., Nelson, N. B., Radionov, V. F., Duarte, C. M., Losno, R., Sciare, J., Voss, K. J.,
1039 Kinne, S., Nalli, N. R., Joseph, E., Krishna Moorthy, K., Covert, D. S., Gulev, S. K., Milinevsky,
1040 G., Larouche, P., Belanger, S., Horne, E., Chin, M., Remer, L. A., Kahn, R. A., Reid, J. S., Schulz,
1041 M., Heald, C. L., Zhang, J., Lapina, K., Kleidman, R. G., Griesfeller, J., Gaitley, B. J., Tan, Q.,
1042 and Diehl, T. L.: Maritime aerosol network as a component of AERONET – first results and
1043 comparison with global aerosol models and satellite retrievals, *Atmos. Meas. Tech.*, 4, 583–597,
1044 doi:10.5194/amt-4-583-2011, 2011.
- 1045 Söderman, D., and Dulac, F.: Monitoring and prediction of the atmospheric transport and deposition
1046 of desert dust in the Mediterranean region, World Meteorological Organization Publication WMO
1047 TD864, Geneva, 177–182, 1998.
- 1048 Tanré, D., Bréon, F. M., Deuzé, J. L., Dubovik, O., Ducos, F., François, P., Goloub, P., Herman, M.,
1049 Lifermann, A. and Waquet, F.: Remote sensing of aerosols by using polarized, directional and
1050 spectral measurements within the A-Train: the PARASOL mission, *Atmos. Meas. Tech.*, 4, 1383–
1051 1395, doi:10.5194/amt-4-1383-2011, 2011.
- 1052 Torres, B., Dubovik, O., Fuertes, D., Schuster, G., Cachorro, V. E., Lapyonok, T., Goloub, P., Blarel,
1053 L., Barreto, A., Mallet, M., Toledano, C., and Tanré, D.: Advanced characterisation of aerosol size
1054 properties from measurements of spectral optical depth using the GRASP algorithm, *Atmos.*
1055 *Meas. Tech.*, 10, 3743–3781, <https://doi.org/10.5194/amt-10-3743-2017>, 2017.



- 1056 Wang, J., C. Zhu, and Y. Zhu, Estimating the POLDER sensitivity to aerosol size using PARASOL
1057 observations, *Remote Sens. Lett.*, 6, 88–96, doi:10.1080/2150704X.2015.1007247, 2015.
1058 Wendisch, M., and J.-L. Brenguier, *Airborne Measurements for Environmental Research*, Wiley-
1059 VCH., 2013.
1060 Zerefos, C. S., Kourtidis, K. A., Melas, D., Balis, D., Zanis, P., Katsaros, L., Mantis, H. T., Repapis,
1061 C., Isaksen, I., Sundet, J., Herman, J., Bhartia, P. K., and Calpini, B.: Photochemical Activity and
1062 Solar Ultraviolet Radiation (PAUR) modulation factors: An overview of the project, *J. Geophys.*
1063 *Res. Atmos.*, 107, doi:10.1029/2000JD000134, 2002.
1064

1065 **Figure captions**1066 **Figure 1.** Map of the location of the 17 AERONET ground-based stations considered in this work.

1067 **Figure 2.** Iterative data inversion procedure to retrieve from airborne observations the aerosol optical
1068 depth (AOD, AOD_F and AOD_C) and Angstrom exponent (AE) as measured by POLDER-3. Green
1069 boxes indicate the input values from airborne measurements (size distribution, scattering and
1070 extinction coefficients) and the initial values of the complex refractive indices estimated from published
1071 literature. The iterative steps of the procedure are indicated in the blue boxes. The results of optical
1072 calculations (corrected size distribution, scattering and extinction coefficients) are in the orange
1073 boxes.

1074 **Figure 3.** Flight tracks of the ATR 42 aircraft (coloured lines) during the TRAQA (left) and ADRIMED
1075 (right) campaigns. Only flights relevant to this study are presented. The location of the vertical profiles
1076 coincidental, at their lowermost altitude, with a POLDER-3 overpass is shown by a black star.

1077 **Figure 4.** Scatter plots of daily AOD retrieved by POLDER-3 at 865 nm with respect to: (top panel)
1078 coincident and co-located values from the 17 ground-based AERONET sites at 870 nm; (middle
1079 panel) airborne PLASMA sunphotometer operated at 865 nm during ADRIMED; (bottom panel)
1080 results of the optical calculations at 865 nm according to Figure 2 from airborne measurements during
1081 TRAQA and ADRIMED. The solid line is the bisector. The dashed lines represent the limits indicated
1082 by the G_{frac} parameter. The characteristics of the linear correlation (number of points N_b , correlation
1083 coefficient, G_{frac} , RMS and bias) are also reported.

1084 **Figure 5.** Scatter plots of daily AOD_F and AOD_C retrieved by POLDER-3 at 865 nm as a function of
1085 coincident AERONET values at 870 nm for the 17 sites in the western Mediterranean. The solid line
1086 is the bisector. The dashed lines represent the limits indicated by the G_{frac} parameter. The
1087 characteristics of the linear correlation (number of points N_b , correlation coefficient, G_{frac} , RMS and
1088 bias) are also reported.

1089 **Figure 6.** Same as figure 5 for cases corresponding to AERONET retrievals yielding a separation of
1090 the fine and coarse modes of the volume distribution at $D_{cut-off} < 1.0 \mu m$ (left) and days with AERONET
1091 $D_{cut-off} \geq 1.0 \mu m$ (right).

1092 **Figure 7.** Scatter plots of AOD_F (left) and AOD_C (right) retrieved by POLDER-3 at 865 nm and
1093 compared to values obtained by optical calculations from airborne measurements of the particle size
1094 number distribution. Panels, from top to bottom, represent the results of the calculations when varying
1095 the cut-off diameter between 0.4 and 1.0 μm . Characteristics of the linear correlation are also reported
1096 (number of points N_b , correlation coefficient R , RMS and bias). Error bars of in situ measurements
1097 were calculated from the optical calculation and the instrumental uncertainties. The solid line is the
1098 bisector.

1099 **Figure 8.** Scatter plots of the Angström Exponent (AE) retrieved by POLDER-3 between 865 and
1100 670 nm with respect to coincident and collocated values from: (top) the 17 ground-based AERONET
1101 sites between 870 and 675 nm; (middle) airborne PLASMA sun photometer operated at 870 and
1102 675 nm during ADRIMED; (bottom) optical calculations at 865 and 670 nm from particle size number
1103 distributions measured in situ during TRAQA and ADRIMED. Only AERONET values corresponding
1104 to POLDER-3 $AOD > 0.1$ are considered because of large uncertainties in AE at low AOD. To facilitate
1105 the reading, the standard deviations of the AERONET values are not represented. Characteristics of
1106 the linear correlations are also reported (number of points N_b , correlation coefficient R , RMS and
1107 bias).

1108 **Figure 9.** Scatter plot of AE versus AOD retrieved by POLDER-3 (left) and AERONET (right) on
1109 coincidental days ($N=6421$) for the 17 stations of Western Mediterranean Sea. Mean and standard
1110 deviations (in brackets) of AOD obtained by classifying the air masses into pollution (blue, $AE \geq 1.5$),
1111 mixed (green, $0.5 < AE < 1.5$) and desert dust (orange, $AE \leq 0.5$) according to Pace et al. (2006) are
1112 shown.

1113 **Figure 10.** Scatterplot of the fraction of coarse mode optical depth due to non-spherical particles (f_{cns})
1114 retrieved by POLDER-3 and that of total optical depth (f_{ns}) estimated by AERONET. Values are



1115 expressed in percent. Only AERONET data points for which the measured AOD exceeded 0.10 and
1116 the AOD_C represented more than 30% of the total AOD are represented. The solid line is the bisector.
1117 Dashed lines represent the interval of $\pm 25\%$ of agreement between POLDER-3 f_{CNS} and AERONET
1118 f_{NS} .

1119 **Figure 11.** Mean and standard deviations of coarse mode optical depth due to non-spherical particles
1120 measured by POLDER-3 (f_{CNS} , blue) and that of total optical depth estimated by AERONET (f_{NS} , red)
1121 classified into four classes: spherical ($f_{CNS} \leq 25\%$); predominant spherical ($25\% < f_{CNS} \leq 50\%$),
1122 predominant non-spherical ($50\% < f_{CNS} \leq 75\%$); non-spherical ($75\% < f_{CNS} \leq 100\%$). Values are
1123 expressed in percent. Only AERONET data points for which the $AOD > 0.10$ and $AOD_C/AOD > 0.30$
1124 are represented. The black triangles represent the number of points in each classes (the dashed
1125 curves is represented for increased readability).

1126 **Figure 12.** Regional maps of average AOD (top left), AE, (top right), AOD_F (middle left), AOD_C (middle
1127 right), AOD_{CNS} (top left), and AOD_{CS} (bottom right) retrieved by POLDER-3 over the period March
1128 2005-October 2013. Mean and standard deviations are also shown.
1129



1130 **Table captions**

1131 **Table 1.** List of AERONET stations available in the western Mediterranean region with at least one
1132 ocean POLDER pixel ($N_{b_{POL}}$) within 0.5° around the station, together with the number of POLDER-3
1133 vs. AERONET observations (and coincident days in brackets) for the different aerosol products from
1134 March 2005 to October 2013.

1135 **Table 2.** List of vertical profiles made by the ATR 42 aircraft during the TRAQA and ADRIMED
1136 campaigns in coincidence with the passage of POLDER-3. For each profile is indicated: the flight
1137 number, the name of the profile, the date, the time period of the profile, the area covered by the flight,
1138 the geographical coordinates, the minimum and maximum altitude of the flight and then, the hour of
1139 POLDER-3 overpass in UTC.

1140 **Table 3.** Criteria of classification of aerosol layers encountered on the vertical profiles of TRAQA and
1141 ADRIMED, based on nephelometer measurements of the scattering coefficient (σ_{scatt}) at 550 nm and
1142 on its spectral dependence (AE_{scatt}) between 450 and 700 nm.

1143 **Table 4.** Summary of evaluated uncertainties on POLDER-3 advanced aerosol products AOD, AE,
1144 AOD_F, AOD_C, and f_{CNS} . N/A stands for not attributed.
1145



1146 **Table 1.** List of AERONET stations available in the western Mediterranean region with at least one
 1147 ocean POLDER pixel (Nb_{POL}) within 0.5° around the station, together with the number of POLDER-3
 1148 vs. AERONET observations (and coincident days in brackets) for the different aerosol products from
 1149 March 2005 to October 2013.

AERONET station	Latitude, Longitude	Altitude (m)	AERONET period	Nb_{POL}	AOD and AE	AOD _F and AOD _C	f_{CNS} and f_{NS}
					POLDER/AERONET (coincidences)		
Barcelona	41°23'N, 02°07'E	125	04/03/2005 - 10/10/2013	13	1171/2059 (827)	1171/1333 (514)	485/623 (116)
Villefranche-sur-Mer	43°41'N, 07°19'E	130	17/02/2005 - 21/08/2013	9	1097/1589 (641)	1097/999 (359)	470/452 (77)
Toulon	43°08'N, 06°00'E	50	04/03/2005 - 04/12/2010	9	1114/1503 (630)	1114/962 (343)	429/393 (67)
Ersa	43°00'N, 09°21'E	80	09/06/2008 - 11/10/2013	17	1178/1252 (541)	1178/676 (281)	504/240 (37)
Malaga	36°42'N, 04°28'W	40	23/02/2009 - 23/09/2013	10	1193/1359 (539)	1193/1036 (419)	465/377 (53)
Lampedusa	35°31'N, 12°37'E	45	06/03/2005 - 11/10/2013	28	1301/1177 (513)	1301/663 (307)	604/285 (54)
Messina	38°11'N, 15°34'E	15	01/05/2005 - 23/20/2012	9	1119/1340 (507)	1119/739 (281)	538/399 (63)
Roma Tor Vergata	41°50'N, 12°38'E	130	10/03/2005 - 11/10/2013	1	725/1954 (486)	725/1199 (280)	297/683 (66)
Blida	36°30'N, 02°52'E	230	06/03/2005 - 19/02/2012	7	989/1357 (475)	989/813 (280)	427/484 (85)
Burjassot	39°30'N, 00°25'W	30	16/04/2007 - 24/04/2013	1	668/1506 (372)	668/1045 (277)	249/480 (54)
Palma de Mallorca	39°33'N, 02°37'E	10	03/08/2011 - 10/10/2013	11	1136/524 (214)	1136/395 (155)	504/162 (19)
Porquerolles	43°00'N, 06°09'E	22	10/05/2007 - 17/07/2013	11	1106/537 (195)	1106/260 (95)	431/82 (9)
Frioul	43°15'N, 05°17'E	40	07/07/2010 - 11/10/2013	8	1037/481 (162)	1037/324 (118)	373/91 (10)
Gozo	36°02'N, 14°15'E	32	25/02/2013 - 11/10/2013	24	1320/210 (102)	1320/162 (67)	633/90 (9)
Montesoro Bastia	42°40'N, 09°26'E	49	26/07/2012 - 23/07/2013	14	1161/240 (76)	1161/43 (7)	506/12 (1)
Alboran	35°56'N, 03°02'E	15	29/06/2011 - 23/01/2012	29	1392/158 (73)	1392/103 (46)	609/47 (7)
Tizi Ouzou	36°41'N, 04°03'E	133	11/04/2012 - 11/10/2013	5	927/238 (68)	927/98 (26)	399/76 (3)
TOTAL	-	-	-	-	18634/18223 (6421)	18634/11228 (3855)	7923/4976 (730)

1150



1151 **Table 2.** List of vertical profiles made by the ATR 42 during the TRAQA and ADRIMED campaigns in
 1152 coincidence with the passage of POLDER-3. For each profile is indicated: the flight number, the name
 1153 of the profile, the date, the time period of the profile, the area covered by the flight, the geographical
 1154 coordinates, the minimum and maximum altitude of the flight and then, the hour of POLDER-3
 1155 overpass in UTC.

1156

Campaign	Flight ID	Profile ID	Date	Time (UTC)	Area	Geographical span		Altitude span (m asl)	POLDER-3 overpass (UTC)	PLASMA
						Beginning	end			
TRAQA	T-V21	T-V21-S1	27/06/2012	10h31–10h52	Corse	42°59'N–7°43'E	42°59'N–7°41'E	122–3534	14h19	----
	T-V24	T-V24-S1	03/07/2012	15h39–16h08	N-East Barcelona	42°14'N–3°31'E	42°8'N–3°29'E	77–3832	15h03	----
	T-V25	T-V25-S1	04/07/2012	08h32–09h04	South of France–Lion Gulf	41°28'N–6°0'E	41°31'N–6°0'E	100–4444	14h05	----
	T-V26	T-V26-S1		16h08–16h41		42°45'N–4°13'E	42°46'N–4°13'E	128–4684		
	T-V27	T-V27-S1	06/07/2012	09h01–09h26	South of France	42°41'N–5°19'E	42°39'N–5°14'E	115–4723	13h47	----
				T-V27-S3		09h26–11h00	42°39'N–5°15'E	42°42'N–5°19'E		
	T-V28	T-V28-S2		16h20–16h42		42°19'N–7°35'E	42°44'N–6°22'E	60–3784		----
ADRIMED	A-V28	A-V28-S2	14/06/2013	10h19–10h44	East Corse–Sardinia	41°38'N–7°14'E	42°4'N–6°46'E	69–3860	14h56	Yes
	A-V29	A-V29-S1	16/06/2013	08h19–08h32	Balears–Sardinia	39°15'N–9°3'E	39°40'N–8°59'E	6–3877	14h37	Yes
		A-V29-S4		09h46–10h15		39°34'N–4°29'E	39°39'N–4°29'E	52–4521		Yes
	A-V30	A-V30-S1	16/06/2013	11h59–12h10	Balears–Sardinia	39°52'N–4°13'E	39°32'N–3°48'E	93–3240	14:37	Yes
	A-V31	A-V31-S4	17/06/2013	09h41–09h54	Balears–Sardinia	40°11'N–3°59'E	39°52'N–4°13'E	95–2899	15h18	Yes
		A-V32-S1		11h46–12h05		39°52'N–4°13'E	39°56'N–4°36'E	93–4519		Yes
	A-V32	A-V32-S4	19/06/2013	13h30–13h44	Corse–Sardinia	39°32'N–9°10'E	39°16'N–9°2'E	10–3548	15h00	Yes
		A-V33-S2		12h47–13h17		43°01'N–9°23'E	43°1'N–9°20'E	73–4502		Yes
	A-V33	A-V33-S4	28/06/2013	14h46–14h59	Sardinia–Lampedusa	39°15'N–9°24'E	39°15'N–9°4'E	5–3224	14h26	----
		A-V38-S2		12h25–13h30		35°30'N–12°38'E	35°30'N–12°37'E	12–5427		----
	A-V44	A-V44-S1	04/07/2013	12h22–12h33	Gulf of Genoa–Corse–Sardinia	43°02'N–9°15'E	43°2'N–9°19'E	59–3513		----
A-V44	A-V44-S2		14h35–14h51		43°35'N–9°7'E	39°15'N–9°4'E	4–3499	15h11	----	

1157



1158 **Table 3.** Criteria of classification of aerosol layers encountered on the vertical profiles of TRAQA and
1159 ADRIMED, based on nephelometer measurements of the scattering coefficient (σ_{scatt}) at 550 nm and
1160 on its spectral dependence (AE_{scatt}) between 450 and 700 nm.

1161

Aerosol type	$AE_{scatt}(450-700 \text{ nm})$	$\sigma_{scatt} (550 \text{ nm})$
Clean background / maritime	–	< 5 or 10 Mm^{-1}
Desert dust	< 0.5	> 10 Mm^{-1}
Pollution	> 1	
Mixed (dust-dominated)	0.5 – 0.75	> 10 Mm^{-1}
Mixed (pollution-dominated)	0.75 – 1	

1162

1163



1164

1165 **Table 4.** Summary of evaluated uncertainties on POLDER-3 advanced products AOD, AE, AOD_F,
1166 AOD_C, and f_{CNS}, and comparison to previous evaluations. N/A stands for not attributed.

1167

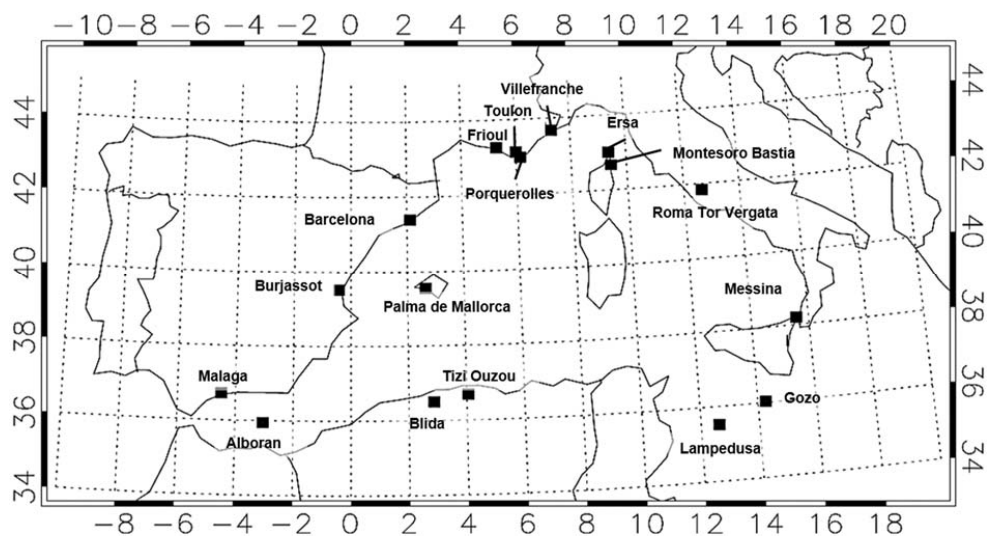
Products	Uncertainties	
	This work	Previous work
AOD	$\Delta AOD = \pm(0.003 + 0.04 \times AOD)$	$\Delta AOD = \pm(0.05 \times AOD + 0.05)^{\S}$
AE	$\Delta AE = \pm(0.11 + 0.44 \times AE)$	$\Delta AE = 0.3-0.5^{\S}$
AOD_F	$\Delta AOD_F = \pm(0.007 + 0.02 \times AOD_F)$	N/A
AOD_F (<i>D</i>_{cut-off} < 1 μm)	$\Delta AOD_F = \pm(0.003 + 0.02 \times AOD_F)$	N/A
AOD_C	$\Delta AOD_C = \pm(0.01 + 0.04 \times AOD_C)$	N/A
f_{CNS}	$\Delta f_{CNS} = \pm 25\%$	N/A
AOD_{CS}	$\Delta AOD_{CS} = AOD_{CS} \times [(0.04 + 0.01/AOD_{CNS})^2 + ((1-\Delta f_{CNS})/(1-f_{CNS}))^2]^{1/2}$	N/A
AOD_{CNS}	$\Delta AOD_{CNS} = AOD_{CNS} \times [(0.04 + 0.01/AOD_{CNS})^2 + (\Delta f_{CNS}/f_{CNS})^2]^{1/2}$	N/A

1168 [§] Tanré et al., (2011) and references therein

1169



1170 **Figure 1.** Map of the location of the 17 AERONET ground-based stations considered in this work.

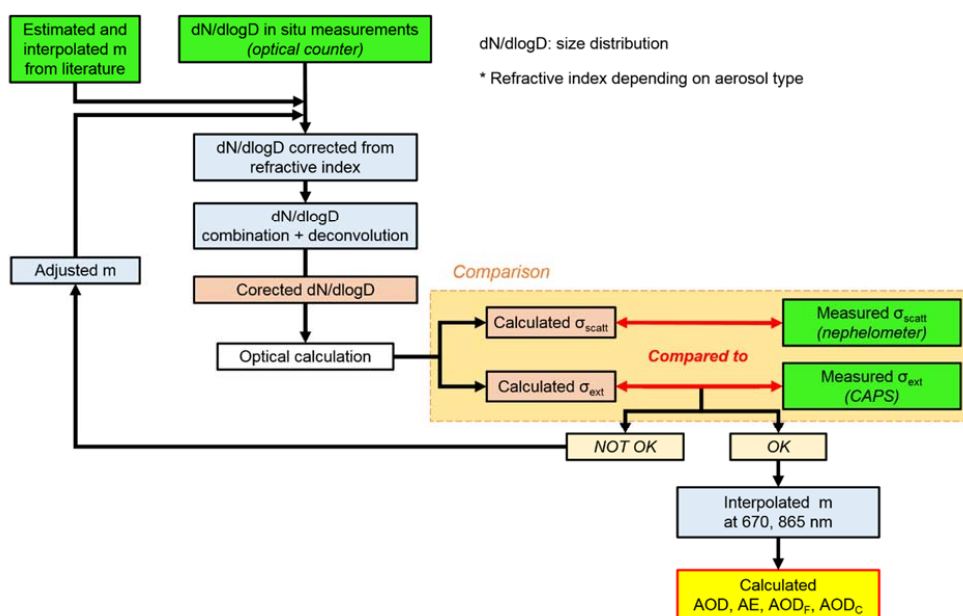


1171

1172



1173 **Figure 2.** Iterative data inversion procedure to retrieve the aerosol optical depth (AOD, AOD_F and
 1174 AOD_C) and Angstrom exponent (AE) measured by POLDER-3 from airborne observations. Green
 1175 boxes indicate the input values from airborne measurements (size distribution, scattering and
 1176 extinction coefficients) and the initial values of the complex refractive indexes estimated from
 1177 published literature. The iterative steps of the procedure are indicated in the blue boxes. The results
 1178 of optical calculations (corrected size distribution, scattering and extinction coefficients) are in the
 1179 orange boxes.
 1180

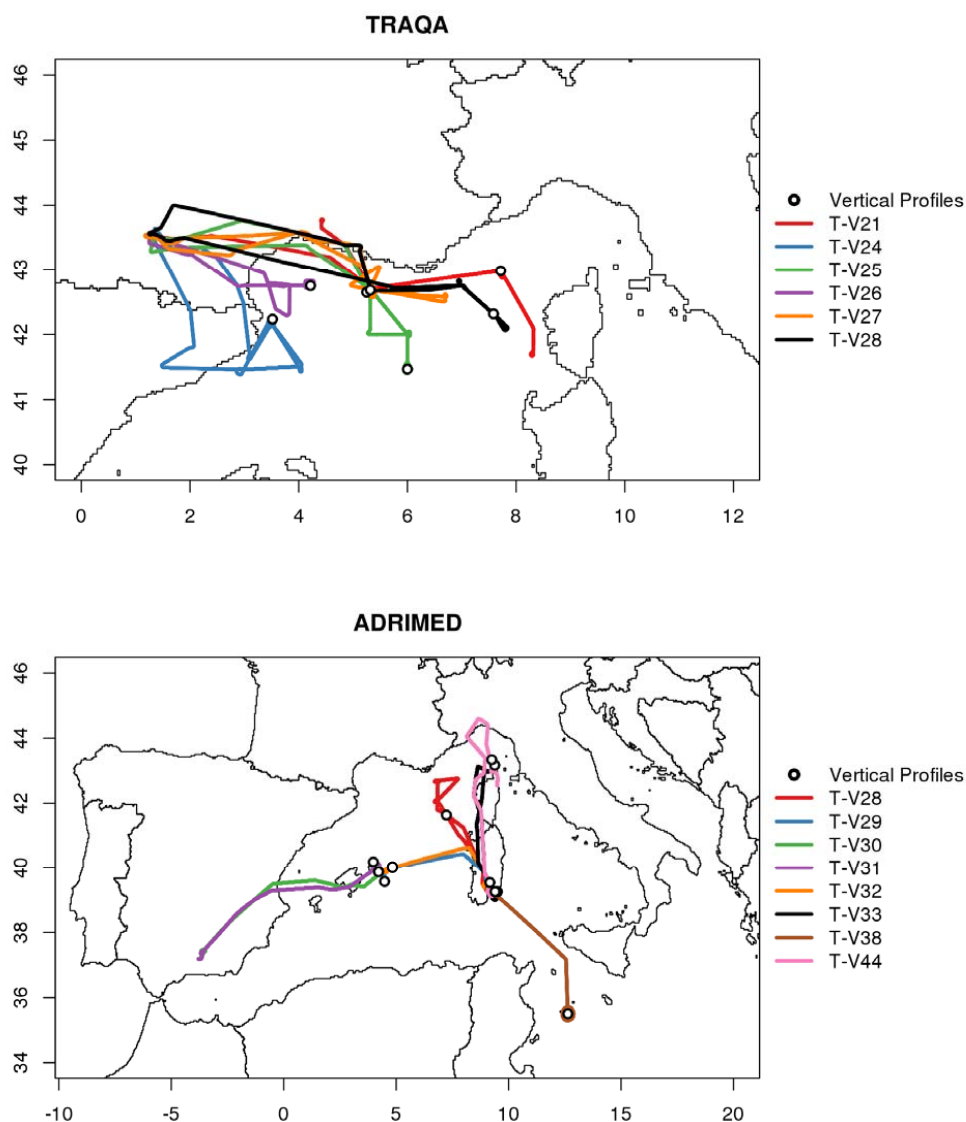


1181

1182



1183 **Figure 3.** Flight tracks of the ATR 42 aircraft (coloured lines) during the TRAQA and ADRIMED
 1184 campaigns. Only flights relevant to this study are presented. The location of the profiles coincidental,
 1185 at their lowermost altitude, with a POLDER-3 overpass is shown by a circle. During the TRAQA
 1186 campaigns, 7 profiles were retained for comparison on 6 flights. During the ADRIMED campaign, 12
 1187 profiles occurring during 9 flights were retained. In this second case, symbols are not always visible
 1188 as overlapping.

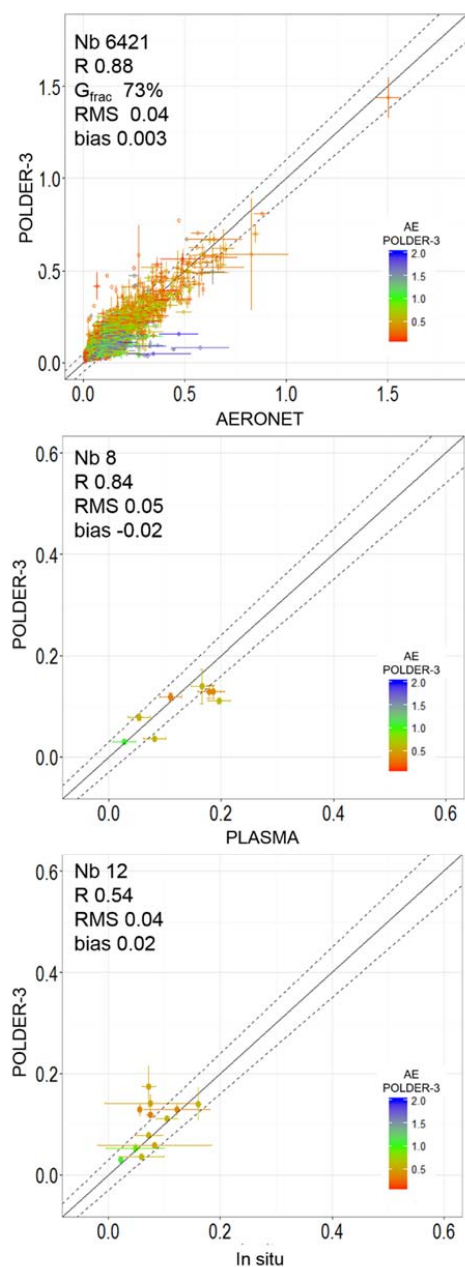


1189

1190



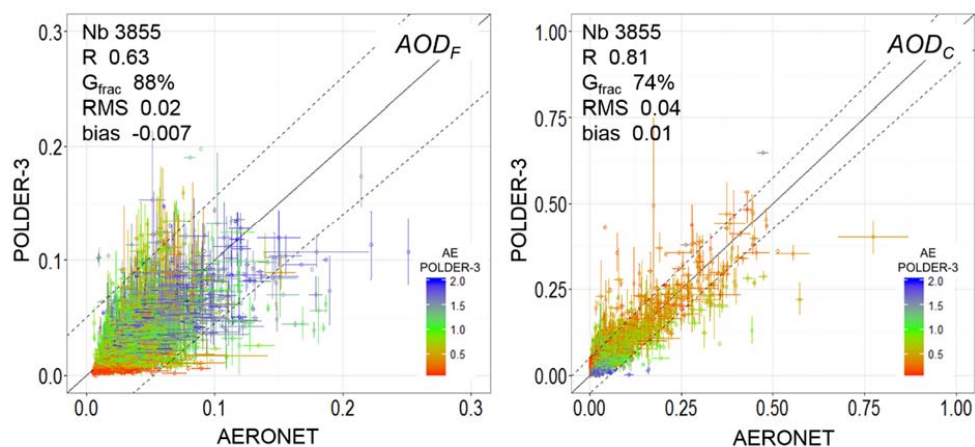
1191 **Figure 4.** Scatterplots of daily AOD retrieved by POLDER-3 at 865 nm with respect to: (top panel)
 1192 coincident and co-located values from the 17 ground-based AERONET sites at 870 nm; (middle
 1193 panel) airborne PLASMA sunphotometer operated at 865 nm during ADRIMED; (bottom panel)
 1194 results of the optical calculations at 865 nm according to Figure 1 from airborne measurements during
 1195 TRAQA and ADRIMED. The solid line is the bisector. The dashed lines represent the limits indicated
 1196 by the G_{frac} parameter. The characteristics of the linear correlation (number of points, correlation
 1197 coefficient, G_{frac} , RMS and bias) are also reported.



1198



1199 **Figure 5.** Scatter plots of daily AOD_F and AOD_C retrieved by POLDER-3 at 865 nm as a function of
 1200 coincident AERONET values at 870 nm for the 17 sites of Western Mediterranean Sea. The solid line
 1201 is the bisector. The dashed lines represent the limits indicated by the G_{frac} parameter. The
 1202 characteristics of the linear correlation (number of points, correlation coefficient, G_{frac} , RMS and bias)
 1203 are also reported.



1204

1205

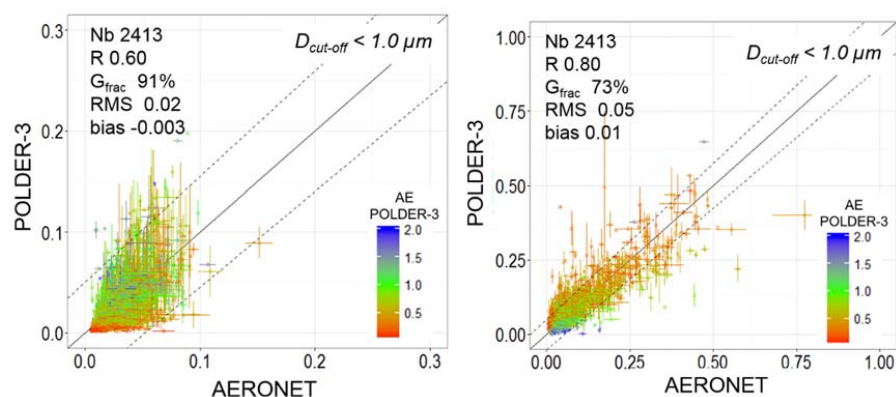
1206



1207 **Figure 6.** Scatter plots of daily AOD_F (top) and AOD_C (bottom) retrieved by POLDER-3 at 865 nm as
 1208 function of coincident AERONET values at 870 nm at the 17 sites of Western Mediterranean Sea for
 1209 cases corresponding to AERONET retrievals yielding a separation of the fine and coarse modes of
 1210 the volume distribution at $D_{cut-off} < 1.0 \mu m$ (left) and days with AERONET $D_{cut-off} \geq 1.0 \mu m$ (right). The
 1211 solid line is the bisector. The dashed lines represent the limits indicated by the G_{frac} parameter. The
 1212 characteristics of the linear correlation (number of points, correlation coefficient R , G_{frac} , RMS and
 1213 bias) are also reported.

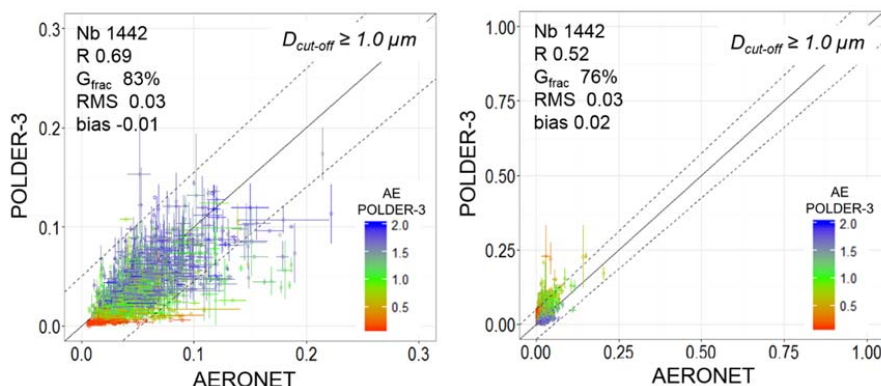
1214

1215 **(a) AOD_F**



1216

1217 **(b) AOD_C**

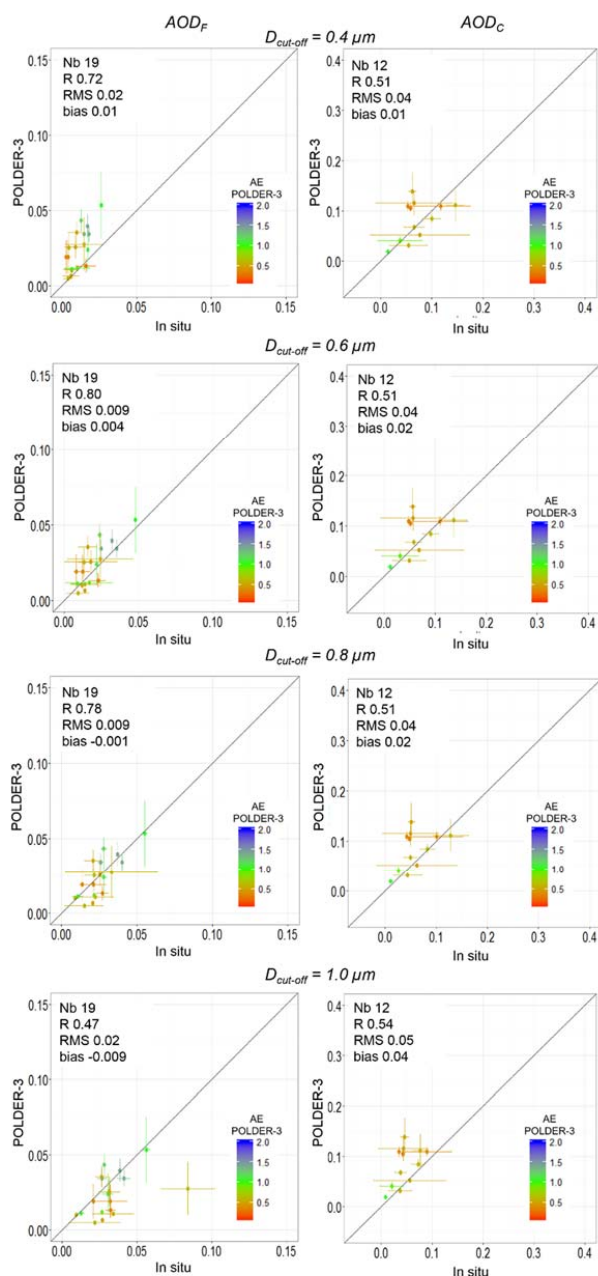


1218

1219



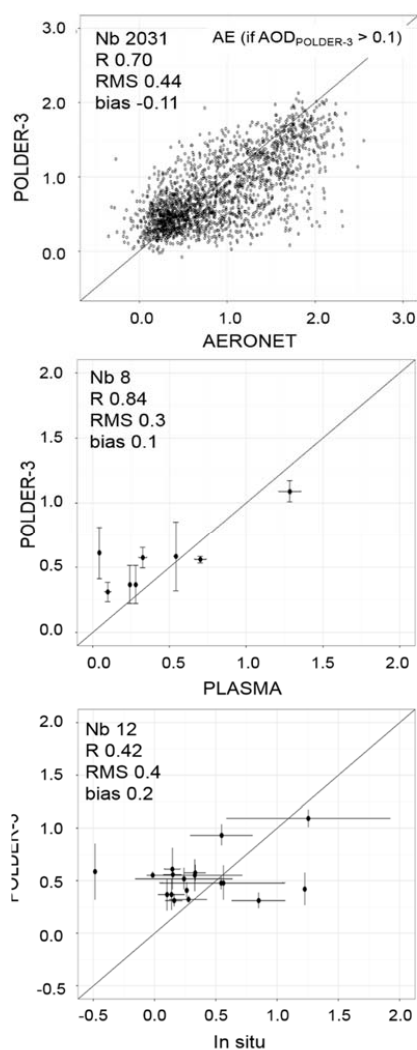
1220 **Figure 7.** Scatter plots of AOD_F (left) and AOD_C (right) retrieved by POLDER-3 at 865 nm and
 1221 compared to values obtained by optical calculations from airborne measurements of the number size
 1222 distribution. Panels, from top to bottom, represent the results of the calculations when varying the cut-
 1223 off diameter between 0.4 and 1.0 μm . Characteristics of the linear correlation are also reported
 1224 (number of points, correlation coefficient R, RMS and bias). Error bars of in situ measurements were
 1225 calculated from the optical calculation and the instrumental uncertainties. The solid line is the bisector.



1226



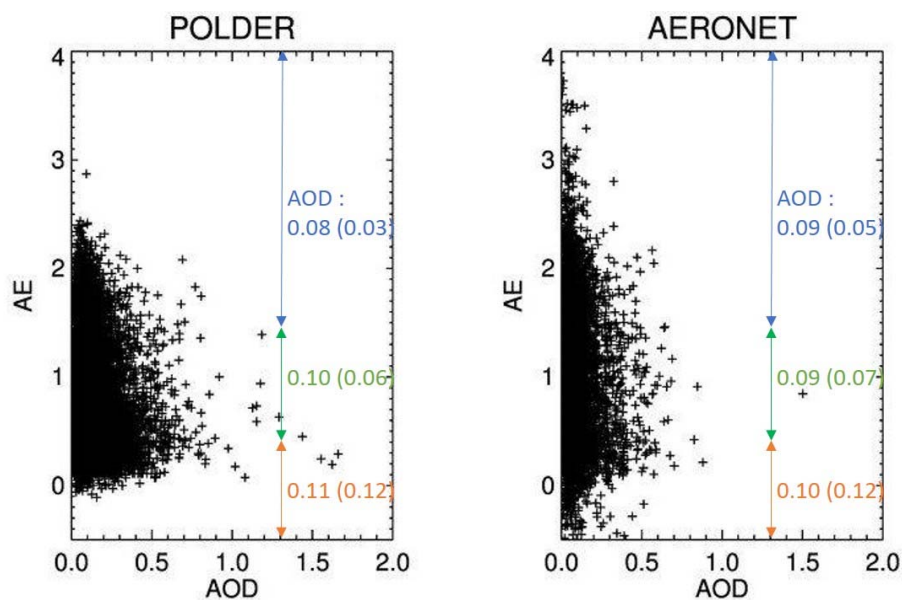
1227 **Figure 8.** Scatter plots of the Angström Exponent (AE) retrieved by POLDER-3 between 865 and 670
 1228 nm with respect to coincident and collocated values from (top) the 17 ground-based AERONET sites
 1229 between 870 and 675 nm; (middle) airborne PLASMA sunphotometer operated at 870 and 675 nm
 1230 during ADRIMED; (bottom) optical calculations at 865 and 670 nm from number size distributions
 1231 measured in situ during TRAQA and ADRIMED. Only AERONET values corresponding to POLDER-3
 1232 AOD larger than 0.1 are considered. To facilitate the reading, the standard deviations of the
 1233 AERONET values are not represented. Characteristics of the linear correlations are also reported
 1234 (number of points, correlation coefficient R , RMS and bias).



1235



1236 **Figure 9.** Scatter plot of AE versus AOD retrieved by POLDER-3 (left) and AERONET (right) on
 1237 coincidental days (N=6421) for the 17 stations of Western Mediterranean Sea. Mean and standard
 1238 deviations (in brackets) of AOD obtained by classifying the air masses into pollution (blue, $AE \geq 1.5$),
 1239 mixed (green, $0.5 < AE < 1.5$) and desert dust (orange, $AE \leq 0.5$) according to Pace et al. (2006) are
 1240 shown.

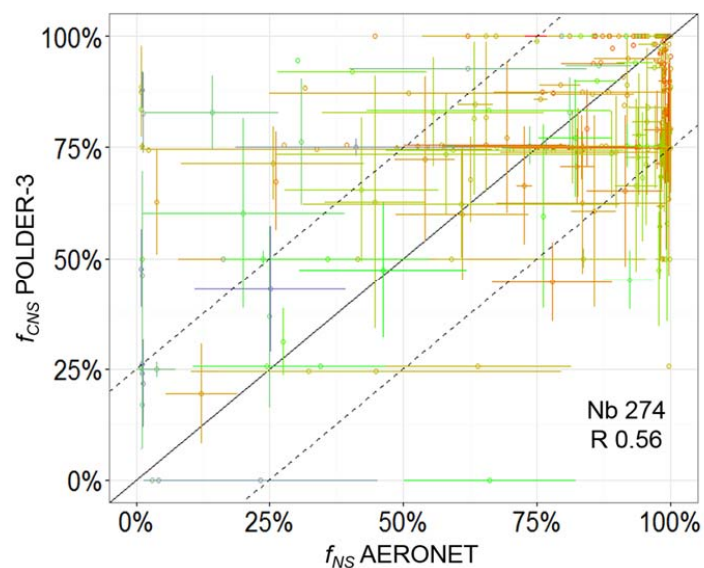


1241

1242



1243 **Figure 10.** Scatterplot of the fraction of coarse mode optical depth due to non-spherical particles (f_{cns})
 1244 retrieved by POLDER-3 and that of total optical depth (f_{ns}) estimated by AERONET. Values are
 1245 expressed in percent. Only AERONET data points for which the measured AOD exceeded 0.10 and
 1246 the AOD_c represented more than 30% of the total AOD are represented. The solid line is the bisector.
 1247 Dashed lines represent the interval of $\pm 25\%$ of agreement between POLDER-3 f_{cns} and AERONET
 1248 f_{ns} .



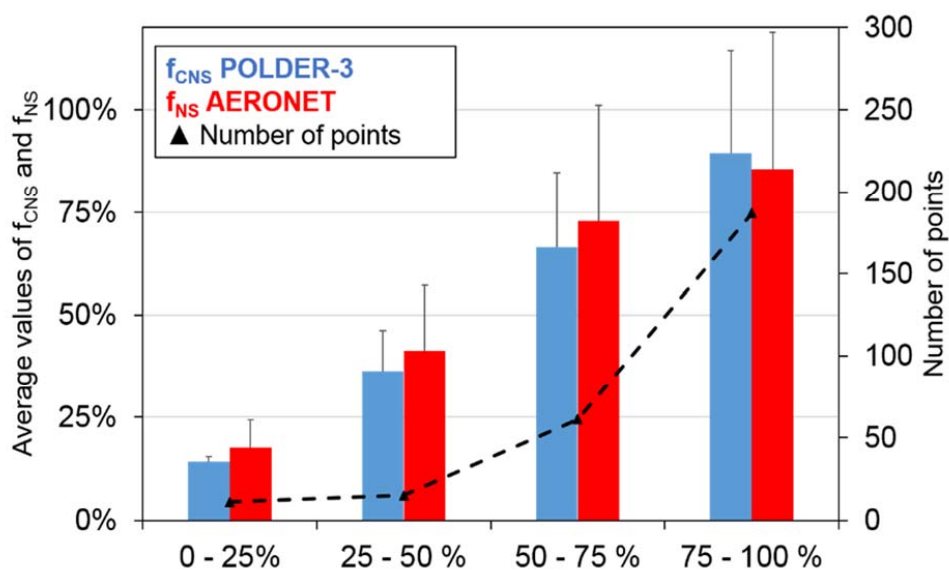
1249

1250



1251 **Figure 11.** Mean and standard deviations of coarse mode optical depth due to non-spherical particles
 1252 measured by POLDER-3 (f_{cns} , blue) and that of total optical depth estimated by AERONET (f_{ns} , red)
 1253 classified into four classes: spherical ($f_{\text{cns}} \leq 25\%$); predominant spherical ($25\% < f_{\text{cns}} \leq 50\%$),
 1254 predominant non-spherical ($50\% < f_{\text{cns}} \leq 75\%$); non-spherical ($75\% < f_{\text{cns}} \leq 100\%$). Values are
 1255 expressed in percent. Only AERONET data points for which the $\text{AOD} > 0.10$ and $\text{AOD}_c/\text{AOD} > 0.30$
 1256 are represented. The black triangles represent the number of points in each classes (the dashed
 1257 curves is represented for increased readability).

1258

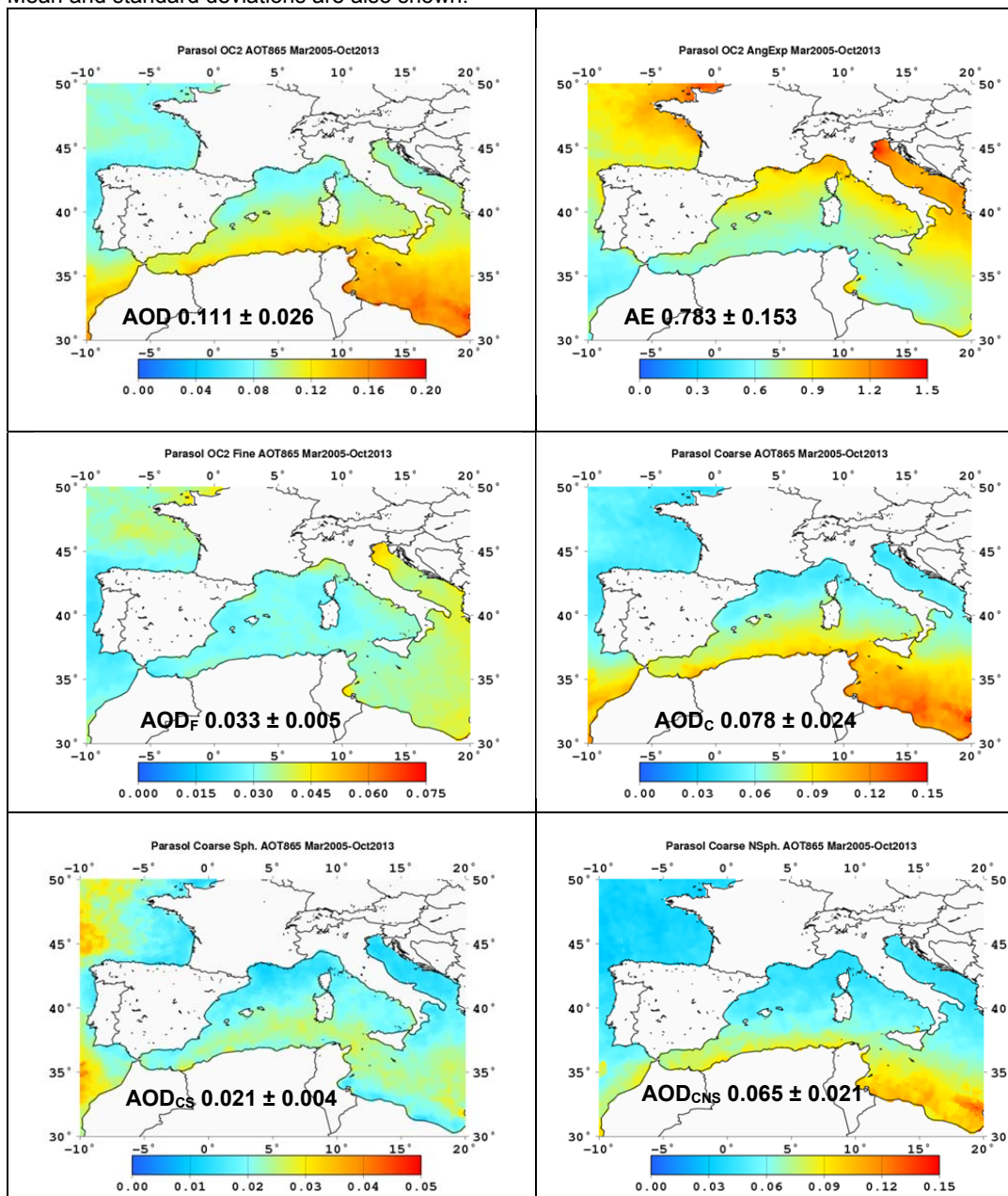


1259

1260



1261 **Figure 12.** Regional maps for AOD, AE, AOD_F (top panel from left to right), AOD_C, AOD_{CNS} and AOD_{CS}
 1262 (bottom panel from left to right) retrieved by POLDER-3 for the period March 2005–October 2013.
 1263 Mean and standard deviations are also shown.



1264

1265